AN ABSTRACT OF THE THESIS OF

Douglas N. Woods for the degree of Master of Science in Nuclear Engineering presented on February 18, 2016

Title: High Order Finite Elements S_N Transport in X-Y Geometry on Meshes with Curved Surfaces in the Thick Diffusion Limit

Abstract approved:

Todd S. Palmer

The high-order finite element S_N transport equations are solved on several test problems to investigate the behavior of the discretization method on meshes with curved edges in X-Y geometry. Simpler problems ensured the correct implementation of MFEM, the general finite element library employed. A convergence study using the method of manufactured solutions demonstrates the convergence rate as a function of number of unknowns for meshes whose sides are described by polynomial curves of increasing order. Optically thick and diffusive problems indicate the DGFEM transport solution trends toward a numerical solution of the diffusion equation, though a rigorous diffusion limit analysis has not yet been performed. A direct solve approach to computing the angular flux unknowns simultaneously is presented as an alternative to source iteration that involves linear algebraically inverting the “streaming plus

collision minus scattering" operator. These results serve as a proof-of-concept of this spatial discretization method.

High Order Finite Elements S_N Transport in X-Y Geometry on Meshes with Curved Surfaces in the Thick Diffusion Limit

by
Douglas N. Woods

A THESIS

submitted to

Oregon State University

in partial fulfillment of
the requirements for the
degree of

Master of Science

Presented February 18, 2016
Commencement June 2016

Master of Science thesis of Douglas N. Woods presented on February 18, 2016.

APPROVED:

Major Professor, representing Nuclear Engineering

Head of the School of Nuclear Science and Engineering

Dean of the Graduate School

I understand that my thesis will become part of the permanent collection of Oregon State University libraries. My signature below authorizes release of my thesis to any reader upon request.

Douglas N. Woods, Author

ACKNOWLEDGEMENTS

I want to thank my major advisor, Dr. Todd Palmer, for piquing my interest in transport discretizations during the advanced courses he taught. He found and presented the opportunity to work on this project, brought immense knowledge, and has been encouraging throughout this entire project. Thanks to Dr. Tom Brunner for serving as my mentor during a summer at Lawrence Livermore National Laboratory and giving me an inordinate amount of time and patience. I credit him for the majority of the implementation of the present work. Also, thanks to Dr. Teresa Bailey for providing a wealth of knowledge and experience to this project and facilitating the logistics. Finally, my family, and specifically my parents, have been so encouraging, supporting, and loving during my life including my academic journey.

TABLE OF CONTENTS

LIST OF FIGURES

LIST OF TABLES

High Order Finite Elements S_N Transport in X-Y Geometry on Meshes with Curved Surfaces in the Thick Diffusion Limit

1 Introduction

The conservation of neutral particle radiation is of particular importance in a variety of applications — reactor physics, astrophysics, radiation detection and protection, and nuclear fusion, for example. Nuclear fusion presents a challenge in computing the distribution of radiation in high energy density physics (HEDP) regime. Drake [1] defines these regimes as having material pressures about 100 GPa or higher.

The field of hydrodynamics investigates the compression, movement, and physical state of high energy density fluids. In these situations, fluids are generally modeled as compressible. Some of the aforementioned physical situations have high density fluids subject to the laws of compressible hydrodynamics. One hydrodynamic simulation code is BLAST[1] [2], which is being developed by a team of scientists at Lawrence Livermore National Laboratory (LLNL). BLAST solves the Euler equations using a high order finite element spatial discretization to evolve the conservation of mass, energy, and momentum. MFEM [3], a general finite element library also developed at LLNL, is employed by BLAST and allows the use of meshes with curved surfaces.

Nuclear fusion applications give rise to very high radiation field densities that can compress and deposit momentum to the fluid [4]. The field of radiation hydrodynamics exists to describe and address these particular challenges in HEDP scenarios. The combination of radiation transport with hydrodynamics helps to fully characterize the compression, motion, and energy of a fluid. BLAST is not yet capable of simulating radiation hydrodynamics. The topic of this thesis is radiation transport in HEDP problems.

Modern radiation transport codes fall into two categories: deterministic and stochastic. The latter rely on statistical methods to converge on a solution. These methods track a particle in a problem domain throughout its lifetime. The particle

---

[1] `https://computation.llnl.gov/project/blast/`

is randomly “born” in a region and followed through its “random walk” as it interacts with material until it either escapes the domain of interest or is absorbed. It is impractical to model all of the particles that exist in some real world problems so an average particle behavior is calculated by tracking enough particles until a statistically significant result is achieved. This can be very accurate but is typically very computationally intensive. There are many Monte Carlo codes available, some of which are listed in Kirk [6].

Deterministic radiation transport methods solve a conservation equation — the radiation transport equation — for the radiation flux. The equation includes the mechanisms for gaining and losing radiation in a given phase space. That is, the radiation flux increases from volumetric sources, radiation streaming into a volume, and from collisions into a phase space. The loss mechanisms include radiation leakage out of a volume, absorption, and collisions out of a phase space of interest. In HEDP materials, these mechanisms can be highly dependent on the internal energy (i.e. temperature and mass density) of the material. Accounting for these dependencies by coupling to the energy equations increases the complexity and difficulty of radiation transport calculations [5, 4].

This radiation transport equation has seven independent variables: time, energy, position (3), and direction of travel (2). In simple problems, the radiation transport equation can be solved analytically. However, approximations are typically made and the equation is discretized in each of the independent variables, where any particular combination of the discretized variables is denoted as a phase space. That is, a mesh approximates spatial regions, angular quadrature approximates the directions of travel to a few discrete directions (S_N), energy groups approximate ranges of particle energies, and time is discretized into small time steps to approximate progression through time. As the discretizations are refined, the numerical solution will converge to the exact solution. There are many discretization methods to suit many different applications. The research presented in this thesis solves the steady-state, monoenergetic, S_N radiation transport equation using high order finite elements on meshes with curved surfaces using MFEM.

The remainder of this chapter is organized as follows: Section 1.1 reviews the finite element spatial discretization method applied to the radiation transport equation, and Section 1.2 outlines the remainder of this thesis.

1.1 Finite Element Spatial Discretization

This research utilizes the finite element method (FEM) to discretize the spatial domain. Finite element discretizations of radiation transport were introduced in the 1970s with triangular meshes in two dimensions (2-D) using arbitrary order finite elements [7, 8]. It is common to use triangular elements especially when discretizing curved boundaries. Two early codes that were developed using piecewise linear finite elements, TRIPLET and TRIDENT, were developed by Reed et al. [9] and Seed et al. [10, 11], respectively. The former experimentally found that the discontinuous finite element method (DFEM) is stable when polynomial weight functions are used. Reed et al. [9] also show that the error of a small pure absorbing problem decreases with increasing finite element order up to 4th order and the computation time increases significantly. The finite element method had been proliferating in the structural and mechanical engineering fields for many years prior [12] showing much promise and warranted further research in the radiation transport context.

In the 1980s, additional FEM research was performed for radiation transport. Mordant [13] created the FEM code ZEPHYR that used bilinear basis functions in two dimensions. The author numerically demonstrated this method is a good alternative (considering computational time) to some finite difference codes in that the FEM is more accurate by generally having more unknowns. Johnson and Pitkaranta [14] and Asadzadeh [15] were among the first to perform error estimates of the fully discrete radiation transport equation using discontinuous Galerkin piece-wise linear basis functions in two dimensions.

HEDP problems often involve spatial meshes whose cells can be very optically thick. Materials that are optically thick and diffusive (scattering dominated) pose problems for iterative methods in transport problems. To address the optically thick mesh cell problem, the spatial mesh could be repeatedly refined until the optical thickness of a mesh cell is on the order of a mean free path. While this is often the case in neutron transport problems, it is computationally impractical in thermal radiation transport problems because the number of cells would be prohibitively expensive. Thus, the optical thickness of the cells remains thick and numerical methods must adapt. Alternatively, the thick problem could be approximated by the solution of a diffusion equation with spatial cells that resolve the diffusion length rather than the mean free path. The drawback to using a diffusion equation solver is its inability to model complicated problems with highly absorbing regions, optically thin regions, material boundaries, or any combination thereof.

The first asymptotic analysis of the radiation transport equation into the diffusion limit was performed by Larsen et al. [16]. Thick diffusion limit analysis examines the behavior of the discretization method as the scattering ratio approaches unity and each spatial cell becomes optically thick. Larsen and Morel [17] concluded that the linear discontinuous FEM (LD method) in one dimension (1-D) possesses the diffusion limit and should be sufficiently accurate for most practical applications, having accurate scalar fluxes in the interior and boundary regions. Later, lumped LD (LLD) methods were shown to be accurate in optically thick problems in 1-D in the interior with an unresolved boundary layer [18]. That is, an accurate solution can be achieved in the problem interior without needing to have an accurate boundary layer solution in optically thick media.

For optically thick problems in 2-D on rectangular meshes, Börgers et al. [21] demonstrated that LD methods do not achieve the diffusion limit. However, Adams [22] observed the behavior of bilinear discontinuous finite elements (BLD) in 2- and 3-D in Cartesian geometries in the diffusion limit. He found mass and surface lumping were required for better solution behavior and acknowledged that much more research needs to be performed for multidimensional diffusion limit DFEMs. Palmer and Adams [23] furthered this by analytically and numerically demonstrating that fully-lumped BLD (FLBLD) methods are accurate in optically thick regimes (i.e. boundary layers and the interiors) in 1-D spherical and 2-D cylindrical geometries.

The LD method was implemented into Attila, a 3-D neutron transport code using unstructured tetrahedral meshes. Wareing et al. [24] demonstrated Attila's ability to accurately model complex geometries with a nuclear well-logging test problem. Version 2 of Attila implemented a tri-linear discontinuous FEM (TLD) where McGhee and Wareing [25] state it solves optically thick radiation transport problems, although they acknowledge the potential for negative fluxes. They note some difficulties of unstructured meshes and techniques to handle them: 1) the finite elements are not analytically integrable and were integrated numerically using Gauss quadrature, 2) ordering of the matrices can be mesh dependent so the meshes were assumed to not be very skewed, and 3) difficulty arises with cyclical cells so all cell surfaces were approximated to have an average outward normal vector, essentially approximating the surfaces as planar.

Adams [26] performed an asymptotic DFEM diffusion limit analysis for arbitrary meshes in Cartesian coordinates. While the analytical and numerical results showed the discretized BLD radiation transport equation has the diffusion limit, he noted this asymptotic analysis would need to be performed for each method independently to confirm it has the diffusion limit. The piecewise linear DFEM (PWLD) method on unstructured meshes was concluded to behave similarly to BLD on rectangular grids in the diffusion limit [27]. This was corroborated and furthered by Bailey et al. [28] who demonstrated the flexibility offered by PWLD in the diffusion limit on higher polygonal meshes in cylindrical geometry where LD and BLD can fail. Subsequently, Bailey et al. [29] obtained similar results for piecewise BLD (PWBLD). Morel and Warsa [30] lumped the surface integral in cylindrical geometry and found additional robustness in the BLD method on quadrilateral grids and similarly found lumping useful on triangular meshes [31]. Morel and Warsa [32] investigated tetrahedral meshes using LLD in the diffusion limit with positive preliminary results in the boundary layer with high-aspect ratio grid cells.

Within optically thick cells, an acceleration method is required to achieve source iteration convergence within a reasonable amount of time. Considerable research has gone into diffusion synthetic acceleration (DSA) [19, 20] as a means to quickly converge the scattering source of the S_N radiation transport problem. Particularly, it has been shown that certain problems have very fast convergence as problems become optically thick and diffusive [19].

Performing convergence studies using higher order (up to 4th order) finite elements on unstructured triangular meshes, Wang and Ragusa [33, 34] found convergence rates can approach $p+1$ (where p is the finite element order). The use of higher order finite elements was conceived at the onset of solving the radiation transport equation with FEM. Other authors have also recently investigated higher order finite element methods [20, 35, 36, 37].

High order finite element methods are susceptible to oscillations in the solution, which can result in negative fluxes. In the context of thermal radiation transport, negative fluxes can result in negative temperatures, negative densities, and negative pressures following the imposition of the equations of state. This research does not explicitly investigate methods to prevent negative fluxes so the oscillations are retained as part of the investigation of the methodology [38]. There are three approaches to the treatment of negative fluxes: ad hoc fixups [39], strictly non-negative solution representations [40], and matrix lumping techniques. The first two result in a non-linear system of equations so matrix lumping has received significant attention. For instance, Adams [26] used traditional lumping techniques with BLD, Maginot [41] explored integration methods associated with lumped matrices, and Brunner [42] considered using linear methods in spatial regions where the solutions are susceptible to these oscillations and higher order finite elements elsewhere. Again, lumping is not investigated within this thesis but it is mentioned throughout.

Since there is a discontinuity of basis functions between spatial regions in DGFEM, a boundary condition is required to be applied to each cell. The upwind angular flux at each cell interface is used as the angular flux incident on that interface. Ragusa et al. [43] proposed a modified upwinding scheme that can robustly achieve the diffusion limit for any finite element order by making the upwind flux dependent upon the amount of scattering in that problem domain. The authors acknowledged the need for further research so this method is not implemented here. Adams [26] proposed the upwind interface condition could be used for mesh cells that have curved surfaces. This research numerically investigates the use of meshes with curved surfaces.

1.2 Outline

The remainder of this thesis details the development of the higher-order FEM radiation transport solver and the characterization tests performed. The research objectives are to develop a high order DGFEM S_N code that solves problems on meshes with curved surfaces. An implicit goal is to evaluate the ability of MFEM to work in this regime. The following chapters include the methods used, results of a suite of test problems, and conclusions. Section 2 describes the discretization of the steady-state, monoenergetic radiation transport equation in angle using level-symmetric Gaussian quadrature, derives the discretization in space using the finite element method, discusses the implementation of the finite element library, and describes the suite of test problems to investigate the spatial discretization of the radiation transport equation. The solutions to these test problems serve as a proof-of-concept of this methodology by solving the radiation transport equation on meshes with high order curved surfaces. Section 3 presents the solutions and a short discussion to the suite of problems. Section 4 summarize the findings of this research.

2 Methods

The radiation transport equation is a mathematical representation of the conservation of particles within a multidimensional phase space,

$$\begin{aligned}\frac{1}{v}\frac{\partial\psi\left(\boldsymbol{r},E,\boldsymbol{\Omega},t\right)}{\partial t}+\boldsymbol{\Omega}\cdot\boldsymbol{\nabla}\psi\left(\boldsymbol{r},E,\boldsymbol{\Omega},t\right)+\sigma_t\left(\boldsymbol{r},E,t\right)\psi\left(\boldsymbol{r},E,\boldsymbol{\Omega},t\right)\\ =\frac{1}{4\pi}\int_{4\pi}d\Omega'\int_0^\infty dE'\sigma_s\left(\boldsymbol{r},E'\rightarrow E,\boldsymbol{\Omega}'\rightarrow\boldsymbol{\Omega},t\right)\psi\left(\boldsymbol{r},E,\boldsymbol{\Omega},t\right)\\ +\frac{1}{4\pi}S_0\left(\boldsymbol{r},E,\boldsymbol{\Omega},t\right)\end{aligned}\tag{1}$$

with incident boundary condition

$$\psi\left(\boldsymbol{r},E,\boldsymbol{\Omega},t\right)=\psi_{\text{inc}}\left(\boldsymbol{r},E,\boldsymbol{\Omega},t\right),\quad\boldsymbol{r}\in\partial\mathbb{V},\ \boldsymbol{\Omega}\cdot\hat{n}<0\tag{2}$$

where v is the particle velocity, ψ is the angular flux, $\boldsymbol{\Omega}\in 4\pi$ is the unit vector of direction of travel, $\boldsymbol{\nabla}$ is the gradient operator, σ_t is the macroscopic total cross section, σ_s is the macroscopic scattering cross section, S_0 is an arbitrary fixed source, $\hat{n}$ is the outward normal unit vector, and ψ_{inc} is the incident angular flux on the boundary $\partial\mathbb{V}$. The arguments include the spatial location vector, $\boldsymbol{r}\in\mathbb{V}$, where $\mathbb{V}$ describes the problem domain, particle energy, E, particle direction of travel, $\boldsymbol{\Omega}$, and time, t. The $E'\rightarrow E$ and $\boldsymbol{\Omega}'\rightarrow\boldsymbol{\Omega}$ terms describe the scattering from energy E' to E and from direction of travel $\boldsymbol{\Omega}'$ to $\boldsymbol{\Omega}$. The first term in Equation 1 is the time-dependent term. The second is the streaming term, accounting for the particle flow into and out of a region. The third term is the absorption term. On the right hand side of the equation are the scattering source and fixed source terms.

While the time, direction of travel, and energy dependencies are important, this research is focused on discretizing in space. Specifically, $\boldsymbol{r}$ is a function of the three spatial Cartesian coordinates, x, y, and z. Although this discretization method is generalized to three-dimensions in space, this research only considers test problems in one- and two-dimensions.

The finite element discretization method allows for general spatial grid geometry. It is of particular interest for this research to predict flux values on a mesh with curved surfaces, but this method allows for arbitrary geometry. More detail is provided in Section 2.3.

2.1 Time and Energy Discretization

Assuming an energy independence and steady-state conditions, Equation 1 becomes

$$\begin{aligned}\boldsymbol{\Omega} \cdot \boldsymbol{\nabla}\psi\left(\boldsymbol{r}, \boldsymbol{\Omega}\right) + \sigma_t\left(\boldsymbol{r}\right)\psi\left(\boldsymbol{r}, \boldsymbol{\Omega}\right) = &\\ &\frac{1}{4\pi}\int_{4\pi} d\Omega' \ \sigma_s\left(\boldsymbol{r}, \boldsymbol{\Omega}' \rightarrow \boldsymbol{\Omega}\right)\psi\left(\boldsymbol{r}, \boldsymbol{\Omega}'\right) + \frac{1}{4\pi} \ S_0\left(\boldsymbol{r}, \boldsymbol{\Omega}\right)\end{aligned} \tag{3}$$

and Equation 2 becomes

$$\psi\left(\boldsymbol{r}, \boldsymbol{\Omega}\right) = \psi_{\text{inc}}\left(\boldsymbol{r}, \boldsymbol{\Omega}\right), \quad \boldsymbol{r} \in \partial\mathbb{V}, \ \boldsymbol{\Omega} \cdot \hat{n} < 0 \tag{4}$$

Assuming isotropic scattering, there is an equal probability of scattering into any direction, which removes the angular dependence of σ_s,

$$\boldsymbol{\Omega} \cdot \boldsymbol{\nabla}\psi\left(\boldsymbol{r}, \boldsymbol{\Omega}\right) + \sigma_t\left(\boldsymbol{r}\right)\psi\left(\boldsymbol{r}, \boldsymbol{\Omega}\right) = \frac{1}{4\pi} \ \sigma_s\left(\boldsymbol{r}\right)\int_{4\pi} d\Omega' \ \psi\left(\boldsymbol{r}, \boldsymbol{\Omega}'\right) + \frac{1}{4\pi} \ S_0\left(\boldsymbol{r}, \boldsymbol{\Omega}\right) \tag{5}$$

Then, completing the final angular flux integration over all angles in the scattering source term results in the steady-state, mono-energetic, isotropic scattering transport equation

$$\boldsymbol{\Omega} \cdot \boldsymbol{\nabla}\psi\left(\boldsymbol{r}, \boldsymbol{\Omega}\right) + \sigma_t\left(\boldsymbol{r}\right)\psi\left(\boldsymbol{r}, \boldsymbol{\Omega}\right) = \frac{1}{4\pi} \ \sigma_s\left(\boldsymbol{r}\right)\phi\left(\boldsymbol{r}\right) + \frac{1}{4\pi} \ S_0\left(\boldsymbol{r}, \boldsymbol{\Omega}\right) \tag{6}$$

where ϕ is the scalar flux defined by

$$\phi \equiv \int_{4\pi} \psi d\Omega \tag{7}$$

Equations 5 and 6 will both be used to represent the transport equation in this thesis.

2.2 Angular Discretization

This research does not investigate the discretization of the transport equation in direction of travel. The discrete ordinates approximation (also referred to as S_N approximation) in Cartesian coordinates is used. The unit sphere is discretized into a number of solid angles, which are described by direction $\mathbf{\Omega}$, where $\mathbf{\Omega}$ is a function of μ, η, and ξ, the x-, y-, and z-components, respectively. Level-symmetric quadrature sets were used to discretize the angular variable. These were obtained through collaboration with Bailey [44], Lau [45], and Maginot [46]. The quadrature sets were provided in individual text files for the unit sphere. The weights are normalized to 4π, which is common and does not require any further manipulation within the solver to adjust to the number of spatial dimensions. Tables 1 and 2 show example S_4 and S_8 level-symmetric quadrature sets, respectively, for the positive octant. These quadratures are reflectioned into the other octants but are omitted for brevity. Other quadrature sets and a general discussion can be found in Lathrop and Carlson [47], and Lewis and Miller [48]. This S_N approximation allows the numerical calculation of the scalar flux from the angular fluxes as

$$\phi \equiv \int_{4\pi} \psi d\Omega \approx \sum_{m=1}^{M} \psi_m \Delta_m \tag{8}$$

where Δ_m is the angular quadrature weight for direction m.

Table 1: S_4 level-symmetric quadrature set for the positive octant.

μ	η	ξ	Δ
3.50021175E-01	3.50021175E-01	8.68890301E-01	5.23598776E-01
3.50021175E-01	8.68890301E-01	3.50021175E-01	5.23598776E-01
8.68890301E-01	3.50021175E-01	3.50021175E-01	5.23598776E-01

Table 2: S_8 level-symmetric quadrature set for the positive octant.

μ	η	ξ	Δ
2.18217890E-01	2.18217890E-01	9.51189731E-01	1.90046963E-01
2.18217890E-01	5.77350269E-01	7.86795792E-01	1.42535222E-01
2.18217890E-01	7.86795792E-01	5.77350269E-01	1.42535222E-01
2.18217890E-01	9.51189731E-01	2.18217890E-01	1.90046963E-01
5.77350269E-01	2.18217890E-01	7.86795792E-01	1.42535222E-01
5.77350269E-01	5.77350269E-01	5.77350269E-01	1.45444104E-01
5.77350269E-01	7.86795792E-01	2.18217890E-01	1.42535222E-01
7.86795792E-01	2.18217890E-01	5.77350269E-01	1.42535222E-01
7.86795792E-01	5.77350269E-01	2.18217890E-01	1.42535222E-01
9.51189731E-01	2.18217890E-01	2.18217890E-01	1.90046963E-01

2.3 Finite Element Spatial Discretization

To discretize using finite elements, the spatial domain is divided by a spatial mesh. Then, the solution is expanded in terms of basis functions. This results in many unknowns and one equation. Each term of the radiation transport equation is multiplied by a weight function $w_{k,i}(\boldsymbol{r})$ and integrated over the volume of mesh cell k, where i indicates the i'th weight function, for $i = 1 \dots J_k$, $\boldsymbol{r} \in \mathbb{V}_k$, and J_k is the number of basis functions. Finally, after applying boundary conditions there are the same number of equations as unknowns. This discretization process is explicitly derived as follows.

First, applying the weighted integrals to Equation 6,

$$\begin{aligned}\int_{\mathbb{V}_k} w_{k,i}\left(\boldsymbol{r}\right)\boldsymbol{\Omega}\boldsymbol{\cdot}\boldsymbol{\nabla}\psi_k\left(\boldsymbol{r},\boldsymbol{\Omega}\right)+\int_{\mathbb{V}_k} w_{k,i}\left(\boldsymbol{r}\right)\sigma_t\left(\boldsymbol{r}\right)\psi_k\left(\boldsymbol{r},\boldsymbol{\Omega}\right)=&\\ \frac{1}{4\pi}\int_{\mathbb{V}_k} w_{k,i}\left(\boldsymbol{r}\right)\sigma_s\left(\boldsymbol{r}\right)\phi_k\left(\boldsymbol{r}\right)+\frac{1}{4\pi}\int_{\mathbb{V}_k} w_{k,i}\left(\boldsymbol{r}\right)S_0\left(\boldsymbol{r}\right)&\end{aligned} \tag{9}$$

Applying Green's Theorem to the streaming term,

$$\begin{aligned}\int_{\mathbb{V}_k} w_{k,i}\left(\boldsymbol{r}\right)\boldsymbol{\Omega}\boldsymbol{\cdot}\boldsymbol{\nabla}\psi_k\left(\boldsymbol{r},\boldsymbol{\Omega}\right)=&\\ \int_{\partial\mathbb{V}_k} w_{k,i}\left(\boldsymbol{r}\right)\hat{n}\left(\boldsymbol{r}\right)\boldsymbol{\cdot}\boldsymbol{\Omega}\;\psi_k\left(\boldsymbol{r},\boldsymbol{\Omega}\right)-\int_{\mathbb{V}_k}\psi_k\left(\boldsymbol{r},\boldsymbol{\Omega}\right)\boldsymbol{\Omega}\boldsymbol{\cdot}\boldsymbol{\nabla}w_{k,i}\left(\boldsymbol{r}\right)&\end{aligned} \tag{10}$$

Substituting this into Equation 9,

$$\begin{aligned}\int_{\partial\mathbb{V}_k} w_{k,i}\left(\boldsymbol{r}\right)\hat{n}\left(\boldsymbol{r}\right)\boldsymbol{\cdot}\boldsymbol{\Omega}\;\psi_k\left(\boldsymbol{r},\boldsymbol{\Omega}\right)-\int_{\mathbb{V}_k}\psi_k\left(\boldsymbol{r},\boldsymbol{\Omega}\right)\boldsymbol{\Omega}\boldsymbol{\cdot}\boldsymbol{\nabla}w_{k,i}\left(\boldsymbol{r}\right)+&\\ \int_{\mathbb{V}_k} w_{k,i}\left(\boldsymbol{r}\right)\sigma_t\left(\boldsymbol{r}\right)\psi_k\left(\boldsymbol{r},\boldsymbol{\Omega}\right)=&\\ \frac{1}{4\pi}\int_{\mathbb{V}_k} w_{k,i}\left(\boldsymbol{r}\right)\sigma_s\left(\boldsymbol{r}\right)\phi_k+\frac{1}{4\pi}\int_{\mathbb{V}_k} w_{k,i}\left(\boldsymbol{r}\right)S_0\left(\boldsymbol{r}\right)&\end{aligned} \tag{11}$$

Expanding the angular and scalar fluxes in terms of basis functions,

$$\psi_k\left(\boldsymbol{r},\boldsymbol{\Omega}\right)=\sum_{j=1}^{J_k} b_{k,j}\left(\boldsymbol{r}\right)\psi_{k,j}\left(\boldsymbol{\Omega}\right) \tag{12}$$

$$\phi_k\left(\boldsymbol{r}\right)=\sum_{j=1}^{J_k} b_{k,j}\left(\boldsymbol{r}\right)\phi_{k,j} \tag{13}$$

and applying them to Equation 11

$$\sum_{j=1}^{J_k} \int_{\partial \mathbb{V}_k} w_{k,i}\left(\boldsymbol{r}\right) \hat{n}\left(\boldsymbol{r}\right) \boldsymbol{\cdot} \boldsymbol{\Omega}\ \psi\left(\boldsymbol{r}, \boldsymbol{\Omega}\right) - \sum_{j=1}^{J_k} \int_{\mathbb{V}_k} b_{k,j}\left(\boldsymbol{r}\right) \psi_{k,j}\left(\boldsymbol{\Omega}\right) \boldsymbol{\Omega} \boldsymbol{\cdot} \boldsymbol{\nabla} w_{k,i}\left(\boldsymbol{r}\right) +$$

$$\sum_{j=1}^{J_k} \int_{\mathbb{V}_k} w_{k,i}\left(\boldsymbol{r}\right) \sigma_t\left(\boldsymbol{r}\right)\ b_{k,j}\left(\boldsymbol{r}\right) \psi_{k,j}\left(\boldsymbol{\Omega}\right) =$$

$$\frac{1}{4\pi} \sum_{j=1}^{J_k} \int_{\mathbb{V}_k} w_{k,i}\left(\boldsymbol{r}\right) \sigma_s\left(\boldsymbol{r}\right) b_{k,j}\ \phi_{k,j} + \frac{1}{4\pi} \int_{\mathbb{V}_k} w_{k,i}\left(\boldsymbol{r}\right) S_0\left(\boldsymbol{r}\right) \quad (14)$$

Applying the finite element discretization to Equation 4, the problem boundary incident flux,

$$\psi\left(\boldsymbol{r}, \boldsymbol{\Omega}\right) \rightarrow \int_{\partial \mathbb{V}_k} w_{k,i}\left(\boldsymbol{r}\right) \hat{n}\left(\boldsymbol{r}\right) \boldsymbol{\cdot} \boldsymbol{\Omega}\ \psi_{\text{inc}}\left(\boldsymbol{r}, \boldsymbol{\Omega}\right), \quad \boldsymbol{r} \in \partial \mathbb{V}, \boldsymbol{\Omega} \boldsymbol{\cdot} \hat{n} < 0 \qquad (15)$$

finishes the finite element discretization.

The finite element equations in matrix form from Adams [26] are adapted here in Equations 16 through 26; his work represents a common starting ground for much of the subsequent FEM transport research. For cell k, weight function i, and basis function j,

$$\left[L_k^{surf} \psi_k^{surf} + L_k \psi_k\right] + T_k \psi_k = \frac{1}{4\pi}\left[T_k - A_k\right] \phi_k + \frac{1}{4\pi} S_{0k} \qquad (16)$$

where,

$$\psi_k(\mathbf{\Omega}) = \left[\psi_{k,1}(\mathbf{\Omega}), \psi_{k,2}(\mathbf{\Omega}), \ldots, \psi_{k,J_k}(\mathbf{\Omega})\right]^T, \tag{17}$$

$$\phi_k = \left[\phi_{k,1}, \phi_{k,2}, \ldots, \phi_{k,J_k}\right]^T, \tag{18}$$

$$\phi_{k,j}(\boldsymbol{r}) \equiv \sum_{m=1}^{M} \Delta_m \psi_{k,j}(\mathbf{\Omega}_m), \tag{19}$$

$$S_{0k} = \left[S_{0_{k,1}}, S_{0_{k,2}}, \ldots, S_{0_{k,J_k}}\right]^T, \tag{20}$$

$$S_{0_{k,j}} \equiv \int_{\mathbb{V}_k} d^3r \ w_{ki}(\boldsymbol{r}) S_0(\boldsymbol{r}), \tag{21}$$

$$\left[L_k^{surf} \psi_k^{surf}\right]_i \equiv \sum_{l=1}^{L_k} \int_{\partial \mathbb{V}_{k,l}} d^2r \ \hat{n}(\boldsymbol{r}_{k,l}) \cdot \mathbf{\Omega} \ w_{k,i}(\boldsymbol{r}) \psi(\boldsymbol{r}_{k,l}, \mathbf{\Omega}), \tag{22}$$

$$[L_k]_{i,j} = -\int_{\mathbb{V}_k} d^3r \ b_{k,j}(\boldsymbol{r}) \mathbf{\Omega} \cdot \boldsymbol{\nabla} \ w_{k,i}(\boldsymbol{r}), \tag{23}$$

$$[T_k]_{i,j} \equiv \int_{\mathbb{V}_k} d^3r \ w_{k,i}(\boldsymbol{r}) \sigma_t(\boldsymbol{r}) b_{k,j}(\boldsymbol{r}), \tag{24}$$

$$[A_k]_{i,j} \equiv \int_{\mathbb{V}_k} d^3r \ w_{k,i}(\boldsymbol{r}) \sigma_a(\boldsymbol{r}) b_{k,j}(\boldsymbol{r}). \tag{25}$$

The cell boundary conditions for the incoming angular flux on interior cells are taken to be the upwind flux,

$$\psi(\boldsymbol{r}_{k,l}, \mathbf{\Omega}) = \begin{cases} \psi\left(\boldsymbol{r}_{k,l}^{-}, \mathbf{\Omega}\right), & \hat{n}(\boldsymbol{r}_{k,l}) \cdot \mathbf{\Omega} > 0 \\ \psi\left(\boldsymbol{r}_{k,l}^{+}, \mathbf{\Omega}\right), & \hat{n}(\boldsymbol{r}_{k,l}) \cdot \mathbf{\Omega} < 0 \end{cases} \tag{26}$$

which enforces a continuous flux between cells. That is, for internal cell k, the angular flux at cell edge l is taken as the upstream value at each surface location $\boldsymbol{r}_{k,l}$. The equations described above are very generalized; they work on an arbitrary spatial grids in one-, two-, or three-dimensions. Additional boundary conditions are needed for the outer surface of the problem domain. Dirichlet, periodic, and reflecting boundaries are used in the suite of test problems introduced below. The weight and basis functions are equal for Galerkin methods (i.e., $w_{k,i} = b_{k,j}$), ensuring that the residuals are orthogonal to the span of the basis functions. This is common practice because (in a particular sense) it minimizes the error introduced by approximating the flux in terms of the basis functions [49]. In this research, these weight and basis functions are allowed to be polynomials of arbitrary order.

2.4 Implementation with MFEM

The open source finite element library Modular Finite Elements Method (MFEM) [3] was used to create the system of linear equations to be solved by a linear algebra solver. The user chooses various parameters to create the system of equations and passes them into MFEM as arguments (i.e. the order of finite elements, the mesh, the number of times to refine the mesh, the order of the mesh, any mesh transformations, the linear algebra solver method, the source iteration convergence criteria, the maximum number of source iterations to perform, the initial guess for the scalar flux, and, in diffusion limit problems, the scaling factor to be applied). MFEM creates the matrices and a linear solver computes the angular flux. This research utilizes the serial version of MFEM and the direct solver UMFPack [50, 51] to solve the equations using a LU decomposition. It is common for transport solvers to solve the local system of equations for an individual spatial cell and sweep through the problem domain to propagate information from one cell to the next. Instead, MFEM creates the system of equations for the entire problem domain and solves for all of the unknowns in all cells simultaneously.

Shown in Table 3 are the functions within MFEM that integrate and assemble the various components of the transport equation (Equation 11) to the linear algebraic system. The functions are displayed along with the general form of their equation and their translation to the applicable component of the transport equation. The last two entries of Table 3 are the interior boundaries using the upstream values (no. 5) and the problem boundary (no. 6). Several of the MFEM equations have coefficients, α and β, that are required input. For item number 1, using $\alpha = 1$ sets the MFEM equation equal to the discretized equation. Similarly, for item number 5 using $\alpha = -1$ and $\beta = 1/2$,

$$\alpha \int_{\partial \mathbb{V}} \boldsymbol{\Omega} \cdot (-\hat{n}) \{\psi\} \, w + \beta \int_{\partial \mathbb{V}} |\boldsymbol{\Omega} \cdot (-\hat{n})| \, [\![\psi]\!] \, w = \int_{\partial \mathbb{V}_k} (\boldsymbol{\Omega} \cdot \hat{n}) \, \psi_k \; w_{k,i} \tag{27}$$

where $\{\psi\} = 1/2 \, (\psi_u + \psi_k)$ and $[\![\psi]\!] = \psi_u - \psi_k$, where ψ_u is the upwind angular flux and ψ_k is the angular flux in cell k.

$$\begin{aligned} -1 \int_{\partial \mathbb{V}} [\boldsymbol{\Omega} \cdot (-\hat{n})] \left[\frac{1}{2} (\psi_u + \psi_k) \right] w + \frac{1}{2} \int_{\partial \mathbb{V}} |\boldsymbol{\Omega} \cdot (-\hat{n})| \, (\psi_u - \psi_k) \, w & \\ = \int_{\partial \mathbb{V}_k} (\boldsymbol{\Omega} \cdot \hat{n}) \, \psi_k \; w_{k,i} & \end{aligned} \tag{28}$$

$$\frac{1}{2} \int_{\partial \mathbb{V}} (\boldsymbol{\Omega} \cdot \hat{n}) \, (\psi_u + \psi_k) \, w + \frac{1}{2} \int_{\partial \mathbb{V}} |\boldsymbol{\Omega} \cdot (-\hat{n})| \, (\psi_u - \psi_k) \, w = \int_{\partial \mathbb{V}_k} (\boldsymbol{\Omega} \cdot \hat{n}) \, \psi_k \; w_{k,i} \tag{29}$$

For $\boldsymbol{\Omega} \cdot \hat{n} < 0$ (incident to cell k),

$$\frac{1}{2} \int_{\partial \mathbb{V}} (\boldsymbol{\Omega} \cdot \hat{n}) \, (\psi_u + \psi_k) \, w - \frac{1}{2} \int_{\partial \mathbb{V}} (\boldsymbol{\Omega} \cdot \hat{n}) \, (\psi_u - \psi_k) \, w = \int_{\partial \mathbb{V}_k} (\boldsymbol{\Omega} \cdot \hat{n}) \, \psi_k \; w_{k,i} \tag{30}$$

$$\frac{1}{2} \int_{\partial \mathbb{V}} (\boldsymbol{\Omega} \cdot \hat{n}) \, \psi_k \; w + \frac{1}{2} \int_{\partial \mathbb{V}} (\boldsymbol{\Omega} \cdot \hat{n}) \, \psi_k \; w = \int_{\partial \mathbb{V}_k} (\boldsymbol{\Omega} \cdot \hat{n}) \, \psi_k \; w_{k,i} \tag{31}$$

The normal vector $\hat{n}$ in MFEM is outward of the upwind mesh surface so a negative was applied to the normal vector to convert it to be the outward normal of the surface of cell k like it has been previously defined in this thesis. Similarly, for item number

6, $\alpha = -1$ and $\beta = -1/2$,

$$\frac{\alpha}{2}\int_{\partial\mathbb{V}} \psi_{\text{inc}}\ \boldsymbol{\Omega}\cdot(-\hat{n})\ \ w - \beta\int_{\partial\mathbb{V}} \psi_{\text{inc}}\,|\boldsymbol{\Omega}\cdot(-\hat{n})|\,w = \int_{\partial\mathbb{V}_k} (\boldsymbol{\Omega}\cdot\hat{n})\,\psi_{\text{inc},k}\ w_{k,i} \tag{32}$$

$$-\frac{1}{2}\int_{\partial\mathbb{V}} \psi_{\text{inc}}\ \boldsymbol{\Omega}\cdot(-\hat{n})\ \ w + \frac{1}{2}\int_{\partial\mathbb{V}} \psi_{\text{inc}}\,|\boldsymbol{\Omega}\cdot(-\hat{n})|\,w = \int_{\partial\mathbb{V}_k} (\boldsymbol{\Omega}\cdot\hat{n})\,\psi_{\text{inc},k}\ w_{k,i} \tag{33}$$

$$\frac{1}{2}\int_{\partial\mathbb{V}} \psi_{\text{inc}}\,(\boldsymbol{\Omega}\cdot\hat{n})\,w + \frac{1}{2}\int_{\partial\mathbb{V}} \psi_{\text{inc}}\,[\boldsymbol{\Omega}\cdot(-\hat{n})]\,w = \int_{\partial\mathbb{V}_k} (\boldsymbol{\Omega}\cdot\hat{n})\,\psi_{\text{inc},k}\ w_{k,i} \tag{34}$$

$$\frac{1}{2}\int_{\partial\mathbb{V}} \psi_{\text{inc}}\,(\boldsymbol{\Omega}\cdot\hat{n})\,w + \frac{1}{2}\int_{\partial\mathbb{V}} \psi_{\text{inc}}\,(\boldsymbol{\Omega}\cdot\hat{n})\,w = \int_{\partial\mathbb{V}_k} (\boldsymbol{\Omega}\cdot\hat{n})\,\psi_{\text{inc},k}\ w_{k,i} \tag{35}$$

MFEM automatically determines the degree of numerical integration to integrate each of the integrals of Table 3. These default integration orders are shown in Table 4. It was discovered that integrating all of the terms consistently was important for numeric conservation. For simplicity, each of the integration orders were set to the largest of the default integration orders. Table 4 shows that the integration order is the same for all of the integrators except DomainLFIntegrator, which is the largest integration order only if $p = 0$ (piecewise constant). While the results presented in this thesis do not consider the circumstance of piecewise constant finite elements, this integration order was included in the code for future use.

MFEM is equipped to visualize data using various tools requiring additional user input. The images presented in this thesis were produced with VisIt, an open source visualization analysis tool [52].

no.	Discretized Equation	MFEM Equation	MFEM Integrator Function
1	$\int_{\mathbb{V}_k} \mathbf{\Omega} \cdot \mathbf{\nabla} \psi_k w_{k,i}$	$\alpha \int_{\mathbb{V}} \mathbf{\Omega} \cdot \mathbf{\nabla} \psi w$	ConvectionIntegrator($\mathbf{\Omega}, \alpha$)
2	$\int_{\mathbb{V}_k} \sigma_t \psi_k w_{k,i}$	$\int_{\mathbb{V}} \sigma_t \psi w$	MassIntegrator(σ_t)
3	$\int_{\mathbb{V}_k} (\sigma_s \phi)\, w_{k,i}$	$\int_{\mathbb{V}} \varphi w$ [1]	DomainLFIntegrator(φ)
4	$\int_{\mathbb{V}_k} S_0 w_{k,i}$	$\int_{\mathbb{V}} S_0 w$	DomainLFIntegrator(S_0)
5	$\int_{\partial \mathbb{V}_k} (\mathbf{\Omega} \cdot \hat{n})\, \psi_k w_{k,i}$	$\alpha \int_{\partial \mathbb{V}} (\mathbf{\Omega} \cdot \hat{n})\, \psi w$ $+\beta \int_{\partial \mathbb{V}} \lvert \mathbf{\Omega} \cdot \hat{n} \rvert\, \psi w$	DGTraceIntegrator($\mathbf{\Omega}, \alpha, \beta$)
6	$\int_{\partial \mathbb{V}_k} (\mathbf{\Omega} \cdot \hat{n})\, \psi_{\mathrm{inc},k} w_{k,i}$	$\frac{\alpha}{2} \int_{\partial \mathbb{V}} \psi_{inc}\, (\mathbf{\Omega} \cdot \hat{n})\, w$ $-\beta \int_{\partial \mathbb{V}} \psi_{inc}\, \lvert \mathbf{\Omega} \cdot \hat{n} \rvert\, w$	BoundaryFlowIntegrator($\psi_{inc}, \mathbf{\Omega}, \alpha, \beta$)

[1] $\varphi \equiv \sigma_s \phi$

Table 3: MFEM PDE function calls where the arguments have been dropped (see Equations 11 and 15 for these details).

Table 4: MFEM default integration orders for transport operators. The notation for the finite element order is p, mesh order is m, and problem dimension is d.

MFEM Integrator	**Default Integration Order**
DGTraceIntegrator	$m \cdot d + 2 \cdot p - 1$
ConvectionIntegrator	$m \cdot d + 2 \cdot p - 1$
MassIntegrator	$m \cdot d + 2 \cdot p - 1$
DomainLFIntegrator	$2 \cdot m$
BoundaryFlowIntegrator	$m \cdot d + 2 \cdot p - 1$

2.5 Solution Methods

Two methods are used to solve for the scalar flux: 1) source iteration and 2) a direct solve of all the angular fluxes simultaneously by inverting the “streaming plus collision minus scattering” operator.

2.5.1 Source Iteration

Source iteration is performed by guessing an initial scalar flux and solving the transport equation for the angular flux in each of the quadrature directions [48]. After multiplying each angular flux by an appropriate quadrature weight and summing over the number of weights, the scalar flux value gets updated and this process is repeated until two subsequent iterations of scalar flux differ by an amount less than a small convergence criteria. The source iteration algorithm for the $(l+1)^{\text{th}}$ iteration is

$$\boldsymbol{\Omega} \cdot \boldsymbol{\nabla} \psi_m^{(l+1)} + \sigma_t \psi_m^{(l+1)} = \frac{1}{4\pi} \sigma_s \phi^{(l)} + \frac{1}{4\pi} S_0 \tag{36a}$$

$$\phi^{(l+1)} \left(\boldsymbol{r} \right) = \sum_{m=1}^{M} \Delta_m \psi_m^{(l+1)} \left(\boldsymbol{r}, \boldsymbol{\Omega} \right) \tag{36b}$$

where M is the number of angular quadrature directions.

Although MFEM has the capability to perform parallel calculations with respect to spatial cells, this transport solver only employs the serial version. However, the source iteration method inherently allows for parallel calculation of angular flux with respect to quadrature angle. Within the $(l+1)^{\text{th}}$ iteration, the M angular fluxes are computed for each angular direction using the same previously determined $(l)^{\text{th}}$ scalar flux. Message Passing Interface (MPI) was employed for this parallel calculation within Equation 36a for each of the M angles. The $(l+1)^{\text{th}}$ calculation of scalar flux is then used back in Equation 36a to perform the next iteration until the convergence criteria is met. A simple convergence criteria is

$$\|\phi^{(l+1)} - \phi^{(l)}\|_\infty < \epsilon_{\text{conv}} \tag{37}$$

where ϵ_{conv} is some small tolerance.

Additional requirements for the convergence criteria are necessary when approaching the diffusion limit (see Section 2.6). Considering a slowly converging scalar flux, Equation 37 will be satisfied if two sequential scalar flux calculations differ by less than ϵ_{conv} even though the scalar flux is not truly converged. To protect against false convergence, the spectral radius, ρ (a measure of the convergence rate), must be taken into account in these situations. It can be estimated with

$$\rho \approx \frac{\|\phi^{(l+1)} - \phi^{(l)}\|_\infty}{\|\phi^{(l)} - \phi^{(l-1)}\|_\infty}, \tag{38}$$

and the modified convergence criteria becomes

$$\|\phi^{(l+1)} - \phi^{(l)}\|_\infty < \epsilon_{\text{conv}} \left(1 - \rho\right) \|\phi^{l+1}\|_\infty, \tag{39}$$

as described by Adams and Larsen [53].

The convergence criteria ϵ_{conv} used for most of the test problems was 10^{-12}. The final difference between iterations upon convergence is much smaller than ϵ_{conv} (up to several orders of magnitude) when accounting for the spectral radius.

2.5.2 Direct Solve of Angular Fluxes

Expanding the scalar flux in terms of angular fluxes and quadrature weights for each cell creates a large system of equations to solve for the angular flux in each direction simultaneously without having to perform any iterations. Expanding the summation of approximation in Equation 8, substituting it into Equation 6 for ϕ, and solving for the angular flux ψ_m in directions $m = 1, \ldots, M$ results in the set of equations

$$\mathbf{\Omega} \cdot \boldsymbol{\nabla} \psi_1 + \sigma_t \psi_1 = \frac{1}{4\pi} \left[\sigma_s \Delta_1 \psi_1 + \cdots + \sigma_s \Delta_m \psi_m + \cdots + \sigma_s \Delta_M \psi_M \right] + \frac{1}{4\pi} S_{0,1} \tag{40a}$$

$$\mathbf{\Omega} \cdot \boldsymbol{\nabla} \psi_2 + \sigma_t \psi_2 = \frac{1}{4\pi} \left[\sigma_s \Delta_1 \psi_1 + \cdots + \sigma_s \Delta_m \psi_m + \cdots + \sigma_s \Delta_M \psi_M \right] + \frac{1}{4\pi} S_{0,2} \tag{40b}$$

$$\cdots$$

$$\mathbf{\Omega} \cdot \boldsymbol{\nabla} \psi_m + \sigma_t \psi_m = \frac{1}{4\pi} \left[\sigma_s \Delta_1 \psi_1 + \cdots + \sigma_s \Delta_m \psi_m + \cdots + \sigma_s \Delta_M \psi_M \right] + \frac{1}{4\pi} S_{0,m} \tag{40c}$$

$$\cdots$$

$$\mathbf{\Omega} \cdot \boldsymbol{\nabla} \psi_M + \sigma_t \psi_M = \frac{1}{4\pi} \left[\sigma_s \Delta_1 \psi_1 + \cdots + \sigma_s \Delta_m \psi_m + \cdots + \sigma_s \Delta_M \psi_M \right] + \frac{1}{4\pi} S_{0,M} \tag{40d}$$

It is clear from Equation 40 that each angular flux is coupled to all of the other angular fluxes. Structuring a block matrix to solve this coupled system of equations is best explained starting with the uncoupled (i.e. no scattering source) system

$$\mathbf{\Omega} \cdot \boldsymbol{\nabla} \psi_m + \sigma_t \psi_m = S_{0,m} \tag{41}$$

Discretizing Equation 41 using the finite element method results in a matrix solve of the form

$$A_m \psi_m = b_m \tag{42}$$

where A_m is the operator that takes into account the streaming and absorption terms of Equation 41 and b_m is the solution vector $S_{0,m}$. Since (in this simplified case) the solution ψ_m is not coupled to other solutions, a large matrix can be formed to solve Equation 42 for all m angular directions simultaneously. For angular quadrature directions $m = 1, \ldots, M$,

$$\begin{bmatrix} A_1 & & & & \\ & A_2 & & & \\ & & A_3 & & \\ & & & \ddots & \\ & & & & A_M \end{bmatrix} \begin{bmatrix} \psi_1 \\ \psi_2 \\ \psi_3 \\ \vdots \\ \psi_M \end{bmatrix} = \begin{bmatrix} b_1 \\ b_2 \\ b_3 \\ \vdots \\ b_M \end{bmatrix} \tag{43}$$

Each ψ_m is the solution vector to all of the support points in the finite element space for quadrature angle m.

The off-diagonal matrices of A in Equation 43 (i.e. the zero matrices) are the matrices that couple each angular flux to the others. Reintroducing the scattering source term by subtracting the scattering term from both sides of Equation 40 (only showing the case for the general m^{th} direction),

$$\mathbf{\Omega} \cdot \boldsymbol{\nabla} \psi_m + \sigma_t \psi_m - [\sigma_s \Delta_1 \psi_1 + \cdots + \sigma_s \Delta_m \psi_m + \cdots + \sigma_s \Delta_M \psi_M] = S_{0,m} \tag{44}$$

Consider a general scattering term from Equation 44,

$$\sigma_s \Delta_m \psi_m \tag{45}$$

Applying the finite element discretization to this term is similar to the absorption term — the angular flux gets expressed in terms of basis functions, multiplied by weight functions, and integrated over the volume. The finite element discretization for Equation 45 creates the full matrix

$$D_m = \begin{bmatrix} \int_{\mathbb{V}} w_1 \sigma_s \Delta_m \psi_{m,1} & \int_{\mathbb{V}} w_1 \sigma_s \Delta_m \psi_{m,2} & \int_{\mathbb{V}} w_1 \sigma_s \Delta_m \psi_{m,3} & \cdots & \int_{\mathbb{V}} w_1 \sigma_s \Delta_m \psi_{m,j} \\ \int_{\mathbb{V}} w_2 \sigma_s \Delta_m \psi_{m,1} & \int_{\mathbb{V}} w_2 \sigma_s \Delta_m \psi_{m,2} & \int_{\mathbb{V}} w_2 \sigma_s \Delta_m \psi_{m,3} & \cdots & \int_{\mathbb{V}} w_2 \sigma_s \Delta_m \psi_{m,j} \\ \int_{\mathbb{V}} w_3 \sigma_s \Delta_m \psi_{m,1} & \int_{\mathbb{V}} w_3 \sigma_s \Delta_m \psi_{m,2} & \int_{\mathbb{V}} w_3 \sigma_s \Delta_m \psi_{m,3} & \cdots & \int_{\mathbb{V}} w_3 \sigma_s \Delta_m \psi_{m,j} \\ \vdots & \vdots & \vdots & \ddots & \vdots \\ \int_{\mathbb{V}} w_i \sigma_s \Delta_m \psi_{m,1} & \int_{\mathbb{V}} w_i \sigma_s \Delta_m \psi_{m,2} & \int_{\mathbb{V}} w_i \sigma_s \Delta_m \psi_{m,3} & \cdots & \int_{\mathbb{V}} w_i \sigma_s \Delta_m \psi_{m,j} \end{bmatrix} \tag{46}$$

for quadrature direction m, where w_i are the weight functions, σ_s is allowed to be spatially dependent, Δ_m is the angular quadrature weight, and $\psi_{m,j}$ is the solution vector for the finite element space that is expanded in terms of basis function j within the integration. Updating Equation 43 with these D_m matrices for each quadrature direction shows that the flux depends on every angular flux at every support point. The result is the large system of equations

$$\begin{bmatrix} A_1 - D_1 & -D_2 & -D_3 & \cdots & -D_m \\ -D_1 & A_2 - D_2 & -D_3 & \cdots & -D_m \\ -D_1 & -D_2 & A_3 - D_3 & \cdots & -D_m \\ \vdots & \vdots & \vdots & \ddots & \vdots \\ -D_1 & -D_2 & -D_3 & \cdots & A_m - D_m \end{bmatrix} \begin{bmatrix} \psi_1 \\ \psi_2 \\ \psi_3 \\ \vdots \\ \psi_m \end{bmatrix} = \begin{bmatrix} b_1 \\ b_2 \\ b_3 \\ \vdots \\ b_m \end{bmatrix} \tag{47}$$

There are

$$N_{\text{unknowns}} = (p+1) \cdot N_{\text{cells}} \cdot N_{\text{angles}} \tag{48}$$

angular flux unknowns in a problem domain, where p is the finite element order, N_{cells} is the number of spatial cells in the mesh, and N_{angles} is the number of quadrature angles. Since this matrix operator has $(N_{\text{unknowns}})^2$ elements, it is easy to see that it can be very large. After solving for the angular fluxes, solving for the scalar flux using Equation 8 is the same as within the source iteration method.

These two solution methods are alternate ways to solve the finite element transport equations. Solving the same problems with each method will help characterize the discretization in various conditions. The direct solve method creates very large matrices so it practically limits the size of the mesh, quadrature, and the finite element order.

2.6 Diffusion Limit

A scaling factor ϵ can be multiplied to each term of the steady-state diffusion equation,

$$-\boldsymbol{\nabla} D \cdot \boldsymbol{\nabla} \phi + \sigma_a \phi = S_0 \tag{49}$$

without affecting the solution to the equation,

$$-\epsilon \boldsymbol{\nabla} D \cdot \boldsymbol{\nabla} \phi + \epsilon \sigma_a \phi = \epsilon S_0 \tag{50}$$

where $D = 1/3\sigma_t$. The scaling factor affects the amount of scattering and absorption that exists at spatial position $\boldsymbol{r}$ [54],

$$\sigma_t \rightarrow \frac{\sigma_t}{\epsilon} \tag{51}$$

$$\sigma_a \rightarrow \epsilon \sigma_a \tag{52}$$

$$S_0 \rightarrow \epsilon S_0 \tag{53}$$

Rather than a truncation analysis, this scaling factor is scaling the physics of the problem. Note that the diffusion equation is invariant to changes in ϵ.

Applying these scaled parameters to Equation 6 results in

$$\boldsymbol{\Omega} \cdot \boldsymbol{\nabla}\psi + \frac{\sigma_t}{\epsilon}\psi = \frac{1}{4\pi}\left(\frac{\sigma_t}{\epsilon} - \epsilon\sigma_a\right)\phi + \frac{\epsilon}{4\pi}S_0 \tag{54}$$

As $\epsilon \to 0$, the problem is scaled to have less absorption and more scattering. The diffusion limit is defined as the limit as $\epsilon \to 0$ of Equation 54, which analytically converges to Equation 49 at $O\left(\epsilon^2\right)$.

This research investigates the discretization schemes discussed above while approaching the diffusion limit for an optically thick medium. Difficulty arises when ϵ is small while solving with the source iteration method. Specifically, as $\epsilon \to 0$, the spectral radius, ρ, approaches unity. Adams and Larsen [53] demonstrated that this affects the iteration counts by

$$\rho^l \geq \frac{\|\psi - \psi^l\|}{\|\psi - \psi^0\|} \tag{55}$$

where l is the current iteration. This says that after many iterations the ratio of the norms of the current error to the first iteration error is bounded by the spectral radius multiplied by itself l times. For instance, to reduce the error by a factor of 1000, the number of source iterations required is

$$\rho^l \geq 0.001 \tag{56}$$

$$l \geq \frac{\ln\rho}{\ln 0.001} \tag{57}$$

Several solutions are tabulated in Table 5 illustrating the computational requirement for these problems.

Table 5: Source iteration convergence iterations.

ρ	l
0.9	66
0.99	687
0.999	6904
0.9999	69,074

2.7 Test Problems

Several test problems were solved for a proof-of-concept and to exercise the transport solver. The first few test problems are very simple problems to serve as early benchmarks. Subsequently, more sophisticated problems were defined including diffusion limit problems, which are a particular focus of this research. Several of the meshes used have curved surfaces. These meshes were created by transforming an orthogonal quadrilateral mesh (Figure 25) — the nodes of the mesh were translated and reconnected with arbitrary order polynomials. For instance, a first order mesh reconnects the translated nodes with linear surfaces (Figure 26), a second order mesh reconnects the translated nodes with quadrilateral surfaces (Figure 27), and so on. Figures 28 and 29 show third and eighth order meshes, respectively.

2.7.1 Test Problem 1: Uniform Infinite Medium with Scattering

This test problem investigates a homogeneous infinite medium with scattering. This infinite medium problem results in a constant solution. An initial scalar flux was chosen ($\phi = 1.4$ cm^{-2} s^{-1}) to test the convergence. It also tested the implementation of the source iteration, angular quadrature, incident flux boundary conditions, high order finite elements on meshes with curves surfaces, conservation, and consistency.

This problem also motivated the work in Table 4.

The following homogeneous material properties describe the problem: $\sigma_t = 1.0$ cm^{-1}, $\sigma_s = 0.3$ cm^{-1}, $\sigma_a = 0.7$ cm^{-1}, and $S_0 = 0.7$ cm^{-2} s^{-1}. The steady-state transport equation then simplifies to

$$\boldsymbol{\Omega} \cdot \boldsymbol{\nabla}\psi\left(\boldsymbol{\Omega}\right) + \sigma_t\psi\left(\boldsymbol{\Omega}\right) = \frac{1}{4\pi}\int_{4\pi} d\Omega'\sigma_s\psi\left(\boldsymbol{\Omega}'\right) + \frac{1}{4\pi}S_0 \tag{58}$$

Because it is a homogeneous infinite medium, $\frac{\partial\psi}{\partial x} = \frac{\partial\psi}{\partial y} = 0$, so,

$$\sigma_t\psi\left(\boldsymbol{\Omega}\right) = \frac{1}{4\pi}\int_{4\pi} d\Omega'\sigma_s\psi\left(\boldsymbol{\Omega}'\right) + \frac{1}{4\pi}S_0 \tag{59}$$

Performing the integration on the right-hand-side,

$$\sigma_t\psi\left(\boldsymbol{\Omega}\right) = \frac{1}{4\pi}\sigma_s\phi + \frac{1}{4\pi}S_0 \tag{60}$$

Integrating over all angles, the exact solution is

$$\phi = \frac{S_0}{\sigma_a} = \frac{0.7}{0.7} = 1.0 \tag{61}$$

$$\psi = \frac{S_0}{4\pi\sigma_a} = \frac{0.7}{0.7\cdot 4\pi} = \frac{1}{4\pi} \tag{62}$$

We use this exact solution as an incident angular flux boundary condition on all four sides of the problem. That is,

$$\psi_{inc} = \frac{S_0}{4\pi\sigma_a} = \frac{1}{4\pi} \tag{63}$$

2.7.2 Test Problem 2: Reed-Hill

The Reed-Hill problem [55, 56] is a one-dimensional, multimaterial test problem with vacuum boundaries. This problem tests the ability of the method to model material interfaces with sharp changes in the flux shape. A two-dimensional mesh with periodic boundary conditions on the top and bottom (Figures 30 and 31) was used to model this one-dimensional problem. Table 6 defines the material regions.

Table 6: *Reed-Hill* problem definition. Units for S_0 are cm^{-2} s^{-1}, and units for σ_t, σ_s, and σ_a are all cm^{-1}.

	$x \in (0,2)$ $x \in (14,16)$	$x \in (2,3)$ $x \in (13,14)$	$x \in (3,5)$ $x \in (11,13)$	$x \in (5,6)$ $x \in (10,11)$	$x \in (6,8)$ $x \in (8,10)$
S_0	0	1.0	0	0	50
σ_t	1.0	1.0	0	5.0	50
σ_s	0	0.9	0	0	0
σ_a	1.0	0.1	0	5.0	50

2.7.3 Test Problem 3: Spatial Convergence study

Using the method of manufactured solutions [57], a spatial convergence study was performed. By substituting the manufactured solution, Equation 64, into Equation 5 and solving for S_0 reveals the fixed source associated with that manufactured solution. Then, the solution to the discretized equations (Equation 16) using this fixed source will converge to the manufactured solution upon refining the spatial mesh or increasing the finite element order of approximation.

Since our approach uses polynomial basis functions, the manufactured solution,

$$\psi\left(x,y,\mu,\eta\right) = a + b\mu + c\eta + d\cos\left(4\pi x\right)\sin\left(3\pi y\right) \tag{64a}$$

$$a = 10 \tag{64b}$$

$$b = 1 \tag{64c}$$

$$c = 5 \tag{64d}$$

$$d = 1 \tag{64e}$$

was chosen to be a function of sine and cosine because it cannot be modeled exactly, where μ and η are components of the angular quadrature, $\mathbf{\Omega}$. The coefficients were chosen to ensure the fixed source and the angular fluxes were positive. The fixed source associated with this manufactured solution is

$$\begin{aligned} S_0 = 4\pi\,(& a\left[\sigma_t - \sigma_s\right] + b\left[\sigma_t\mu\right] + c\left[\sigma_t\eta\right] + d\left[-4\pi\mu\sin\left(4\pi x\right)\sin\left(3\pi y\right) + \right. \\ & \left. 3\pi\eta\cos\left(4\pi x\right)\cos\left(3\pi y\right) + \sigma_t\cos\left(4\pi x\right)\sin\left(3\pi y\right) - \sigma_s\cos\left(4\pi x\right)\sin\left(3\pi y\right)\right]) \end{aligned} \tag{65}$$

The incident angular fluxes for the boundaries of the problem are

$$\psi_{\text{inc}}\left(x,y,\mu,\eta\right) = \begin{cases} a + b\mu + c\eta + d\sin\left(3\pi y\right), & x = 0 \\ a + b\mu + c\eta, & y = 0 \\ a + b\mu + c\eta + d\sin\left(3\pi y\right), & x = 1 \\ a + b\mu + c\eta + d\cos\left(4\pi x\right)\sin\left(3\pi\right), & y = 1 \end{cases} \tag{66}$$

and were derived from Equation 64 by substituting in the appropriate x or y boundary location.

Table 7 shows the case matrix of tests considered, showing finite element orders and the number of spatial cells in the mesh. This case matrix was performed for each of four spatial meshes: orthogonal, first, second, and third order meshes. The unrefined meshes (i.e. 16 mesh cells) are shown in Figures 25 - 28. Two refinements of the orthogonal mesh are shown in Figures 32 and 33, and two refinements of the third order mesh are shown in Figures 34 and 35 for illustration.

Table 7 is populated with the number of unknowns appearing in the problem domain. Specifically, the number of unknowns, $N_{\text{unknowns}} = N_{\text{cells}} \left(p+1\right)^2$, is a function of the number of mesh cells, N_{cells}, and finite element order, p. S_8 level-symmetric quadrature was used in all cases to reduce ray effects and was solved on a unit square where $x, y \in [0,1]$. The L^2 norm of the errors between the discretized solution and the manufactured solution are calculated at each combination of finite element order and mesh refinement on each of the four meshes.

Table 7: Case matrix for convergence study showing the number of unknowns in the problem.

		finite element order				
		1	2	4	6	8
number of mesh cells	16	64	144	400	784	1296
	64	256	576	1600	3136	5184
	256	1024	2304	6400	12,544	20,736
	1024	4096	9216	25,600	50,176	82,944
	4096	16,384	36,864	102,400	200,704	331,776
	16,384	65,536	147,456	409,600	802,816	1,327,104

2.7.4 Test Problem 4: 1-D Diffusion Limit

A two-dimensional homogeneous test problem by Adams [26] is solved to investigate the behavior of high order finite elements on meshes with curved surfaces for cells that are optically thick and diffusive. The problem is defined by $\sigma_t = 1/\epsilon$, $\sigma_a = \epsilon$, $S_0 = \epsilon$ and the Dirichlet boundary conditions $\phi(0) = \phi(1) = 0$, where $\sigma_s = \sigma_t - \sigma_a$. As $\epsilon \to 0$, the discretized transport equation solution converges to the discretized diffusion equation solution, which provides a reference solution to evaluate the accuracy of this methodology.

A one-dimensional version of this problem is considered first. The diffusion equation has an analytical solution in slab geometry and served as the reference solution. Expressing Equation 49 in slab geometry,

$$-\frac{\partial}{\partial x} D(x) \cdot \frac{\partial}{\partial x}\phi(x) + \sigma_a \phi(x) = S_0 \tag{67}$$

Consider the case where D does not depend on x,

$$\frac{\partial^2 \phi(x)}{\partial x^2} - \frac{\sigma_a}{D}\phi(x) = -\frac{S_0}{D} \tag{68}$$

and let $L^2 \equiv D/\sigma_a$,

$$\frac{\partial^2 \phi(x)}{\partial x^2} - \frac{1}{L^2}\phi(x) = -\frac{S_0}{D} \tag{69}$$

The method of undetermined coefficients was used to analytically solve this second order partial differential equation. The equation associated with the homogeneous solution is

$$\frac{\partial^2 \phi(x)}{\partial x^2} e^{1/L^2} - \frac{1}{L^2}\phi(x) e^{1/L^2} = 0 \tag{70}$$

and has the general solution

$$\phi(x) = c_1 e^{x/L} + c_2 e^{-x/L} \tag{71}$$

The equation associated with the particular solution is

$$\phi_P(x) = a \tag{72}$$

Plugging this into Equation 69,

$$0 - \frac{1}{L^2}a = -\frac{S_0}{D} \tag{73}$$

and solving for a,

$$a = \frac{S_0}{\sigma_a} \tag{74}$$

The general solution to Equation 69 becomes

$$\phi(x) = c_1 e^{x/L} + c_2 e^{-x/L} + \frac{S_0}{\sigma_a} \tag{75}$$

Applying the Dirichlet boundary conditions from the problem description to get the analytic diffusion equation solution that served as the reference solution for this test problem,

$$\phi(x) = \frac{S_0}{\sigma_a}\left[\left(\frac{e^{-1/L} - 1}{e^{1/L} - e^{-1/L}}\right)e^{x/L} - \left(\frac{e^{-1/L} - 1}{e^{1/L} - e^{-1/L}} + 1\right)e^{-x/L} + 1\right] \tag{76}$$

For various choices of the scaling factor, $\epsilon = \{0.1, 0.05, 0.01\}$, the L^2 norm of the error between the transport solution and the reference solution was calculated. A one-dimensional mesh was not available so this problem was solved on a two-dimensional mesh with periodic boundary conditions on the top and bottom (Figure 36) to emulate slab geometry.

2.7.5 Test Problem 5: 2-D Diffusion Limit

Using the same physical parameters as Test Problem 4 ($\sigma_t = 1/\epsilon$, $\sigma_a = \epsilon$, and $S_0 = \epsilon$), this problem solved the two-dimensional diffusion limit problem described by Adams [26]. Since there is not an analytic solution, the transport solution was compared to the solution from a diffusion code using the same mesh and finite elements. Using the same values for ϵ as before (i.e. $\epsilon = \{0.1, 0.05, 0.01\}$) the transport solutions were compared to the diffusion equation solution. This was solved on the mesh in Figure 37.

2.7.6 Test Problem 6: Strong Scatter with Discontinuous Boundary Conditions

This problem has been adapted from Test Problem 1 of Palmer [58]. It is homogeneous, optically thick ($c = 0.999$), and is defined by $\sigma_t = 1000$ cm^{-1}, $\sigma_s = 999$ cm^{-1}, and $S_0 = 0.0$ cm^{-2} s^{-1}. There are vacuum boundaries on all sides except for six alternating locations on the problem boundary with an incident angular flux strength of 1.0 cm^{-1} s^{-1} ster^{-1}. Figure 1 shows the problem geometry where red borders indicate the incident flux locations and Figure 38 shows the mesh. This problem illuminated the effects of unresolved boundary layers on the interior solution (sufficiently far from the boundary) in these optically thick regions. That is, the spatial mesh at the top of Figure 1 is less resolved than the mesh on the right side and resulted in more pronounced negative fluxes within those boundary layers.

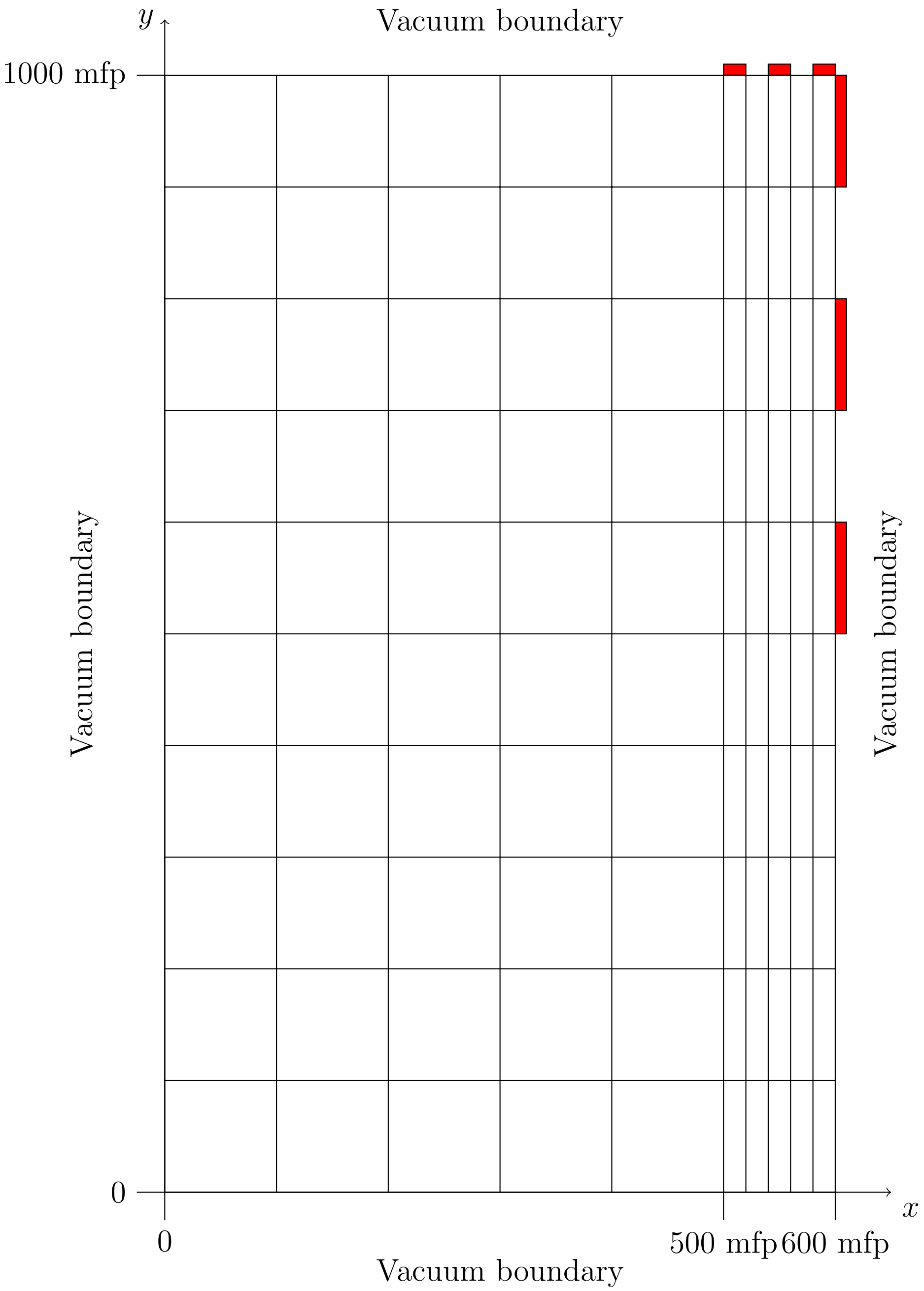

Figure 1: Test Problem 6 problem geometry; red boundaries indicate incident boundary locations.

2.7.7 Test Problem 7: Material Discontinuity Stress Test

This problem was adapted from Test Problem 3 from Palmer [58]. There are five different regions with various absorption and scattering cross sections as described in

Table 8. Figure 2 shows the problem geometry and Figure 39 shows the mesh. There is an incident flux on the left side of strength 1 cm^{-2} s^{-1} ster^{-1} and the remaining boundaries are vacuum. Since thermal radiation transport problems can have opacities that vary over many orders of magnitude, a robust transport code must work in all regimes. This problem begins to test this challenge. Additionally, optically thick regions are more sensitive to anisotropic fluxes in the unresolved boundary layers. The thick absorber attenuates fluxes that are perpendicular to the source-absorber interface less than fluxes at an angle. This creates a preferentially anisotropic flux into the scattering region testing the accuracy of the boundary condition on the interior solution in the diffusive region. Lastly, the angular flux that is mostly unattenuated is allowed to enter the scattering region through the very thin absorbing region. This incident flux enters at a grazing angle testing the boundary condition on the interior solution at this material interface.

Table 8: Test Problem 7 material properties.

Material Region	σ_t cm^{-1}	σ_s cm^{-1}	S_0 cm^{-2} s^{-1}
Source	1.0	1.0	1.0
Very thin absorber	0.0001	0.0	0.0
Thick absorber	10.0	0.0	0.0
Very thick absorber	100.0	0.0	0.0
Very thick scatterer	1000.0	1000.0	0.0

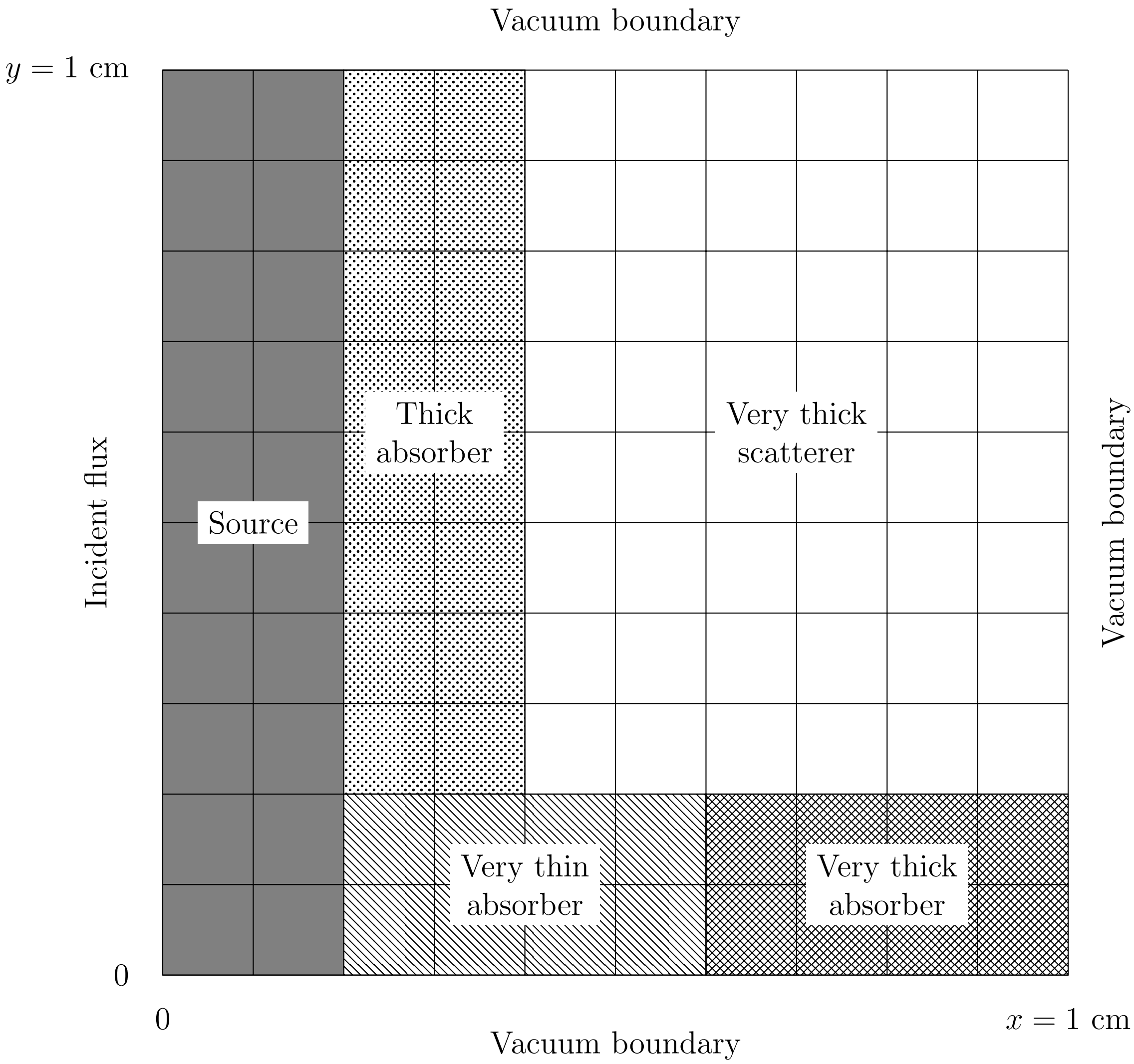

Figure 2: Test Problem 7 problem geometry; materials defined in Table 8.

2.7.8 Test Problem 8: 2-D Diffusion Limit Direct Solve Method

This is the same problem as Test Problem 5 (Section 2.7.5) using the direct solve method described in 2.5.2 for $\epsilon = \{0.1, 0.01, 0.001, 0.0001\}$. The objective was to test the accuracy of the method as the problem approaches the diffusion limit. The transport solution was compared to the diffusion equation solution on the same mesh with the same finite elements. The error was calculated using the L^2 norm of the difference between the transport solution and the reference solution for all of the unknowns. The direct solve method is limited to solving smaller problems (i.e. fewer angular quadrature directions, fewer mesh cells, lower order finite elements) due to the size of the matrix that is generated. The spatial mesh is shown in Figure 40.

3 Results

The results presented in this section are separated into their respective test problems. Problem characteristics and solution methods are discussed along with important conclusions from the problems.

3.1 Test Problem 1: Uniform Infinite Medium With Scattering

This problem is defined in Section 2.7.1. Introducing the scattering term required the implementation of source iteration. Figure 3 shows the DGFEM solution to the transport equation with $\sigma = 1.0$ cm^{-1}, $\sigma_s = 0.3$ cm^{-1}, $S_0 = 0.7$ cm^{-2} s^{-1} ster^{-1}, and $\psi_{\text{inc}} = S_0/\sigma_a$. This calculation was performed using S_8 level-symmetric quadrature, 8th order finite elements, on the mesh in Figure 37. This calculation took 14 iterations with a convergence criteria of $\epsilon_{\text{conv}} = 10^{-12}$. There are 20,736 unknowns on 256 spatial zones. The exact solution, $\phi = 1.0$ cm^{-2} s^{-1} (Equation 62), is shown by the "Max" and "Min" values underneath the scale on the left-hand-side of the figure. This solution demonstrates successful implementation of the source iteration, angular quadrature, incident flux boundary conditions on a high order finite elements on meshes with curved surfaces, conservation, and consistency. It was noted in Section 2.7.1 that this problem motivated the work in Table 4.

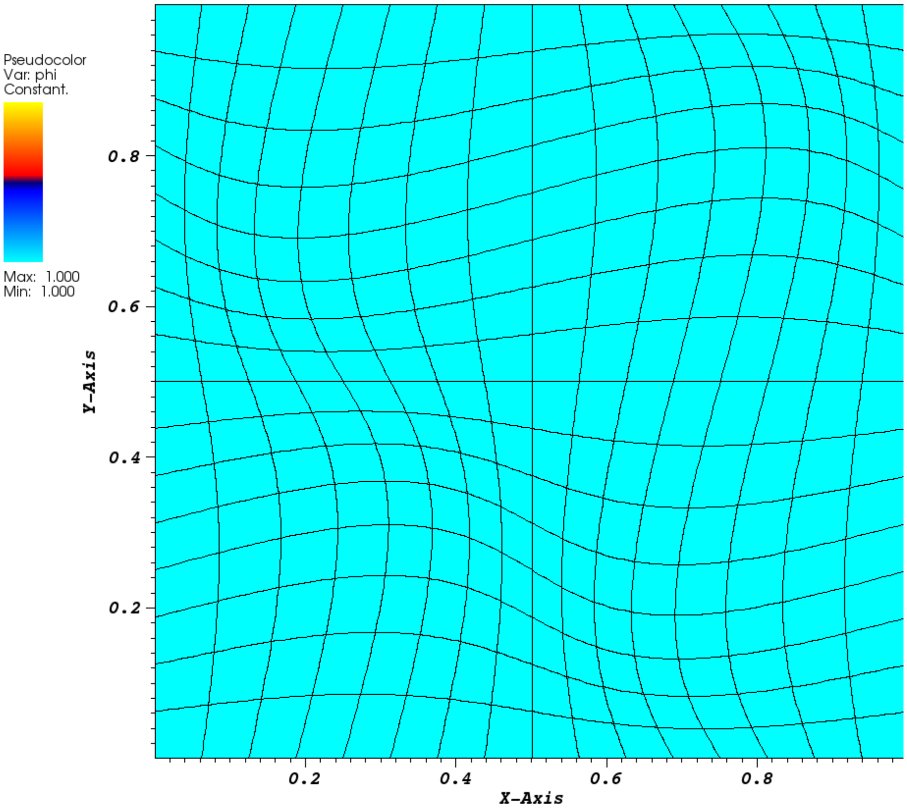

Figure 3: Uniform infinite medium solution with fixed and scattering sources.

3.2 Test Problem 2: Reed-Hill

The Reed-Hill problem [55] is a multiregion problem defined in Section 2.7.2. Rather than modifying the MFEM source code to implement reflecting boundaries, this problem was modeled with the material regions mirrored across $x = 8$ making the domain $x \in [0, 16]$. This problem was solved using S_8 level-symmetric quadrature with 8^{th} order finite elements on two orthogonal meshes: a coarser mesh with a 200 x 3 spatial grid (Figure 30) and a mesh refined to 400 x 3 (Figure 31), both with periodic boundary conditions on the top and bottom to emulate slab geometry. The coarser mesh had 81 unknowns in each of 600 spatial cells. Thus, there were 1800 unknowns along the x-direction. The refined mesh had 3600 unknowns along the x-direction. There were vacuum boundaries at $x = 0$ and $x = 16$. The solution using the refined mesh is shown in Figure 4.

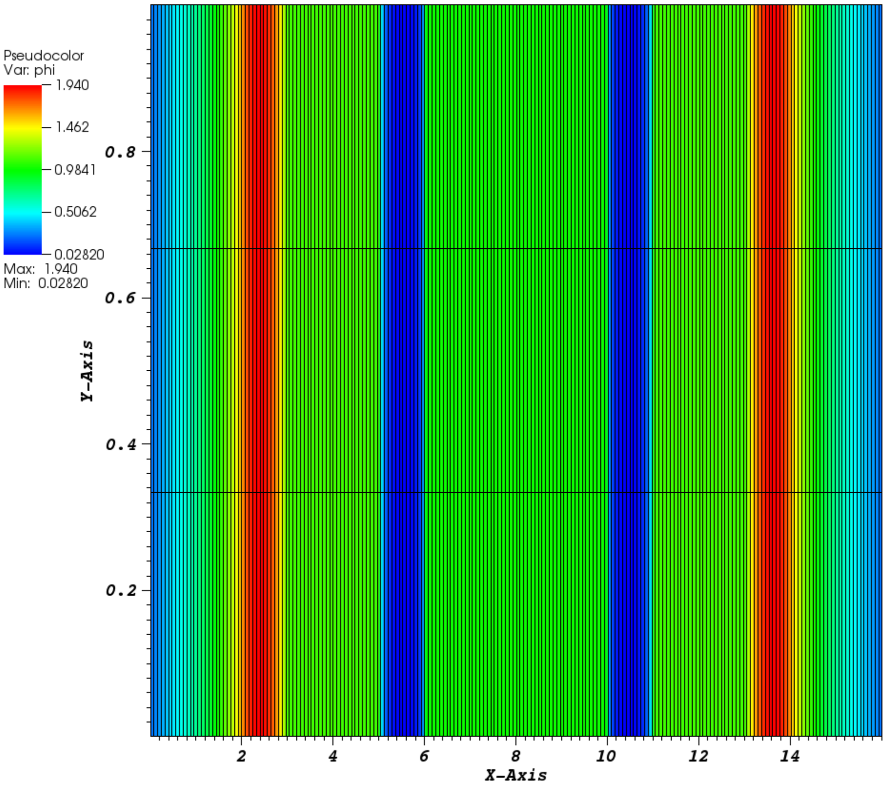

Figure 4: DGFEM Reed-Hill problem solution on a refined 2-D mesh with periodic boundaries on top and bottom (Figure 31) to simulate slab geometry.

Figure 5 shows the scatter plot of all of the scalar fluxes from the solution shown in Figure 4 as a function of their x values. Because there is no spread of data (i.e. each scalar flux at any particular x value lies on the line), the scatter plot demonstrates the solution is indeed one-dimensional.

A lineout was taken from Figure 4 at $y = 0$ and is shown in Figure 6. The discretized transport solution models it smoothly even at the material interfaces where there are sharp changes in the flux. Similarly, a lineout is shown for the coarser mesh in Figure 7. There are some observable oscillations of the discretized transport

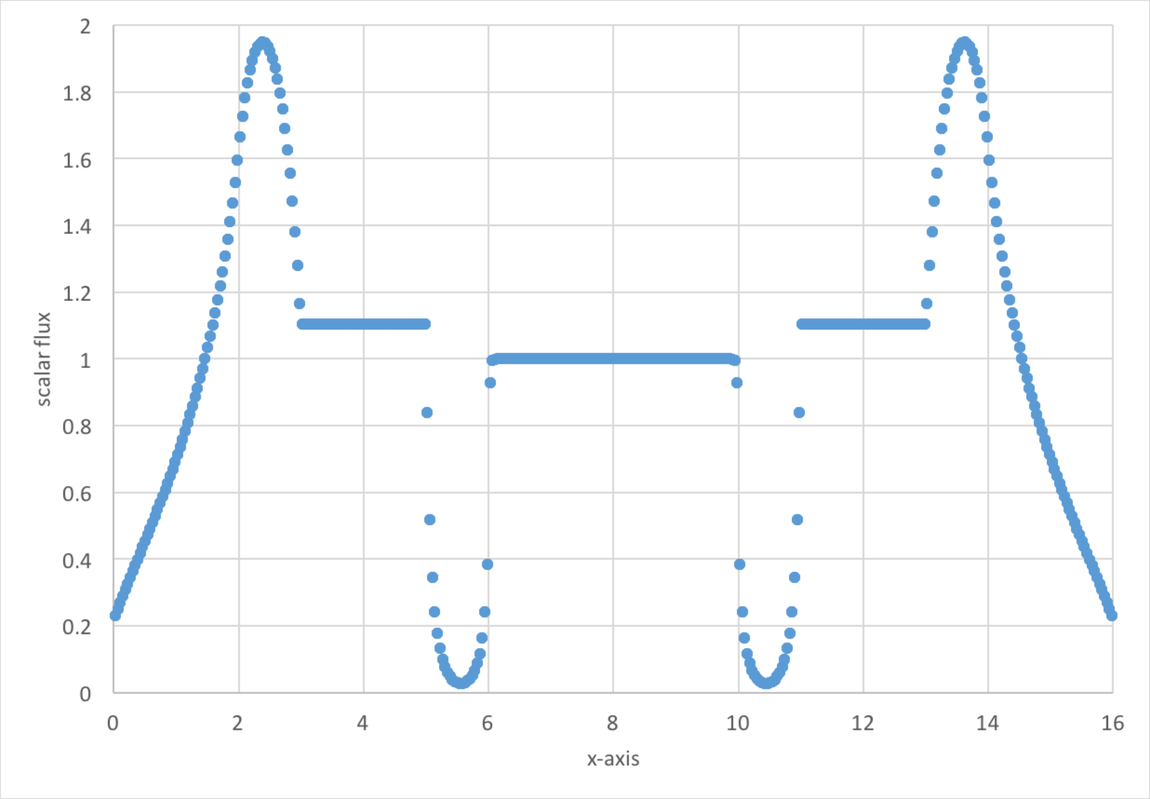

Figure 5: Reed-Hill problem solution scatter plot; each flux value from Figure 4 is plotted against its x-value indicating a true 1-D solution from a 2-D mesh.

solution on the coarser mesh near $x = 3$, $x = 5$, $x = 11$ and $x = 13$, which Gresho and Lee [38] note may indicate that the mesh is inappropriate and requires refinement in those areas.

This problem was also solved with a one-dimensional step differencing transport code with 16,000 spatial cells using the same S_8 level-symmetric angular quadrature; this result serves as the reference solution. The L^2 error from the reference solution for the coarser mesh is 0.0335 and is 0.00181 for the refined mesh, both using a convergence criteria of $\epsilon_{\text{conv}} = 10^{-12}$ implemented through Equation 39. The spectral radius of the source iteration was 0.773 and converged in 101 iterations for the coarser mesh. Similarly, the spectral radius of the source iteration was 0.774 and converged in 102 iterations for the refined mesh.

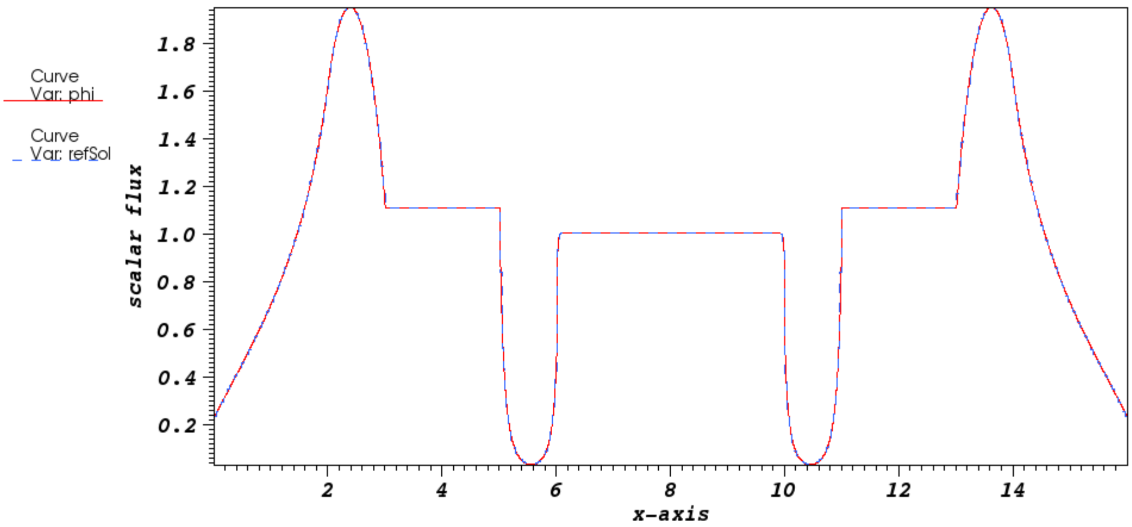

Figure 6: Lineout of Reed-Hill problem solution at $y = 0$ of Figure 4 on mesh with 400 cells across (Figure 31); red is the DGFEM solution and blue is the reference solution.

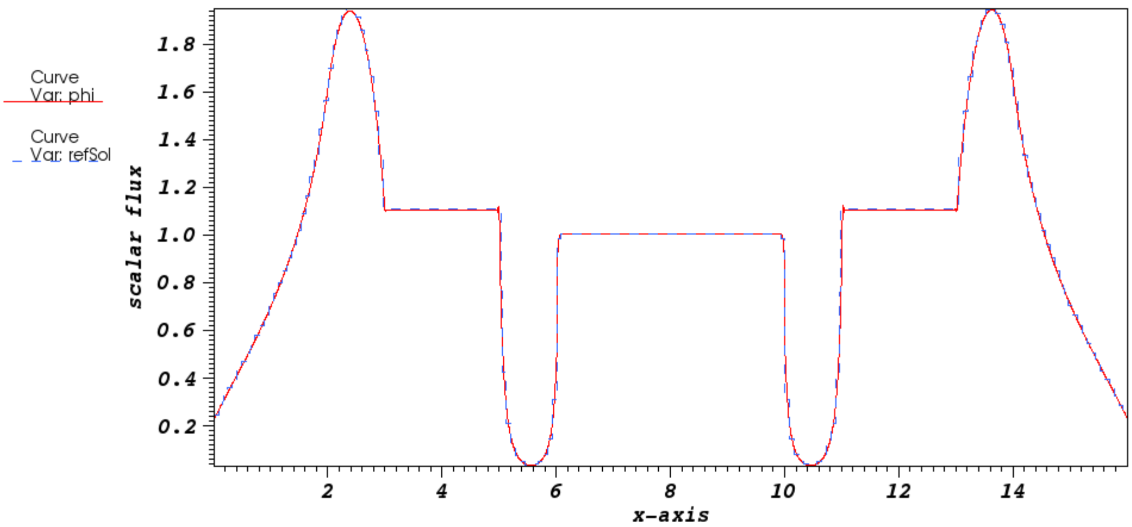

Figure 7: Lineout of Reed-Hill problem solution at $y = 0$ of Figure 4 on mesh with 200 cells across (Figure 30); red is the DGFEM solution and blue is the reference solution.

This problem was a preliminary test for problems involving significant material heterogeneity.

3.3 Test Problem 3: Spatial Convergence Study

This problem is described in Section 2.7.3. The data points in Figures 8 - 11 show the L^2 norm of the difference between the DGFEM scalar flux and the reference solution as a function of the square root of the number of unknowns in the finite element space (the data is found in Tables 10 - 13). Lines connect the values calculated with the same finite element order. The number of unknowns is a function of the number of mesh cells and the order of finite elements,

$$N_{\text{unknowns}} = N_{\text{cells}} \cdot (p+1)^2 \tag{77}$$

where N_{unknowns} is the number of unknowns, and p is the finite element order. Each was calculated with S_8 angular quadrature to reduce the impact of ray effects.

The convergence rates reported in Table 9 were determined from the slopes of the lines in Figures 8 - 11. It is common to report convergences rate as functions of the mesh size. This poses a difficulty because the meshes with curved surfaces are not uniform. Hence, the convergence rates have been reported as a function of the number of unknowns along one axis. The convergence rate on quadrilateral meshes is expected to be $p+1$ [8]. Wang and Ragusa [34] found $p+1$ convergence rates on triangular meshes also. Thus, the results are consistent with theoretical and numerical expectations.

Machine precision prohibited the accurate calculation of errors smaller than on the order of 10^{-14}. Values that were judged to be smaller than this maximum achievable accuracy were omitted from determining the convergence rates. The number of unknowns was limited to available memory so not all of the test cases of Table 7 could be computed. It is clear from Figures 8 - 11 that increasing the number of unknowns in this problem decreases the error, whether by increasing the number of mesh cells or the order of the finite elements. Convergence rates are greater for higher order finite elements. Also, the convergence rates were relatively insensitive to the increasing curvature of the mesh surfaces.

The fixed source term in this manufactured solution is several orders of magnitude greater than the other terms of the transport equation. Brunner [59] found that while this can reveal errors in the source term, it can mask numerical deficiencies in the smaller terms. A more comprehensive study should include changing the magnitude of each term independently.

Table 9: Manufactured solution convergence rates on the square root of N_{unknowns} determined from the slopes of the lines in Figures 8 - 11.

		mesh order			
		orthogonal	1	2	3
element order	1	2.680	2.559	2.709	2.706
	2	3.541	3.384	3.526	3.529
	4	5.729	5.426	5.640	5.627
	6	7.821	7.258	7.641	7.567
	8	9.853	9.052	9.613	9.342

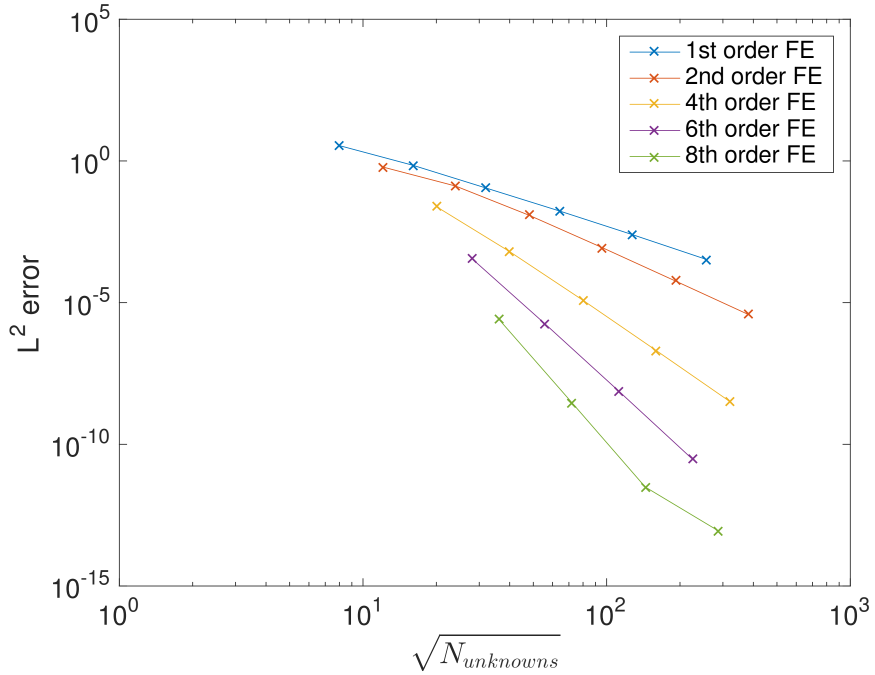

Figure 8: First order orthogonal mesh errors as a function of the square root of N_{unknowns}.

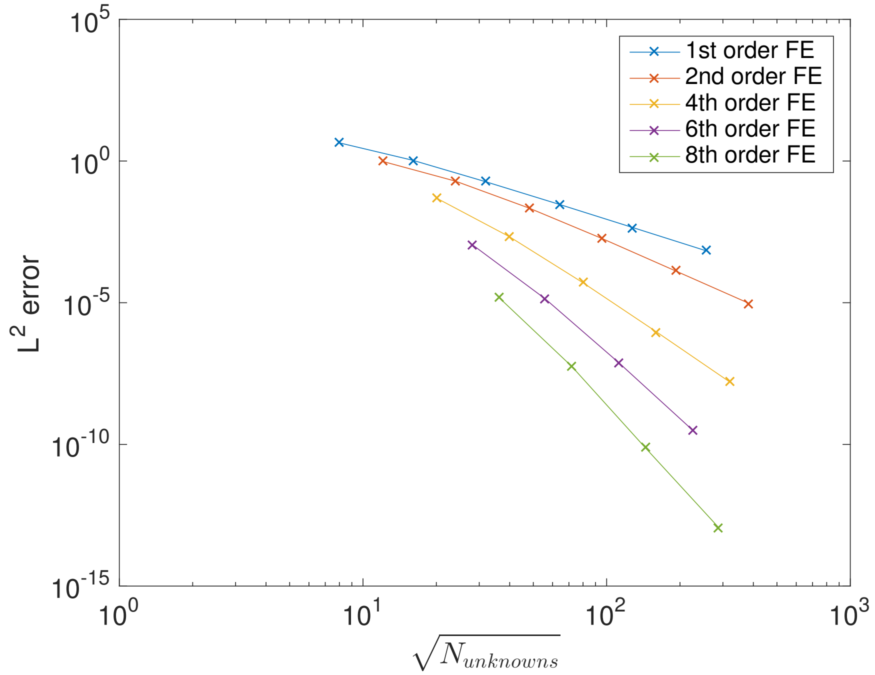

Figure 9: First order transformed mesh errors as a function of the square root of N_{unknowns}.

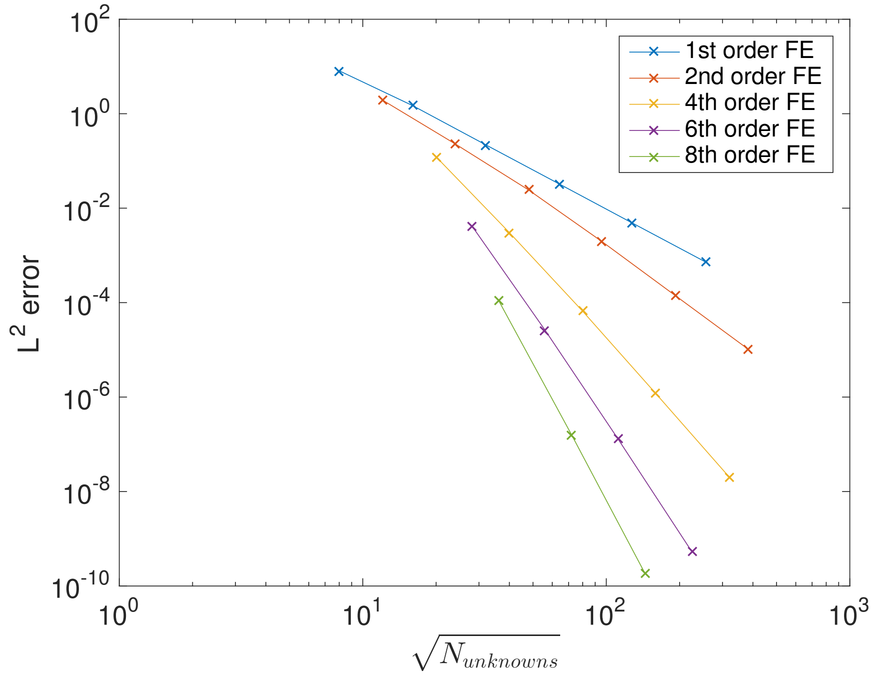

Figure 10: Second order transformed mesh errors as a function of the square root of N_{unknowns}.

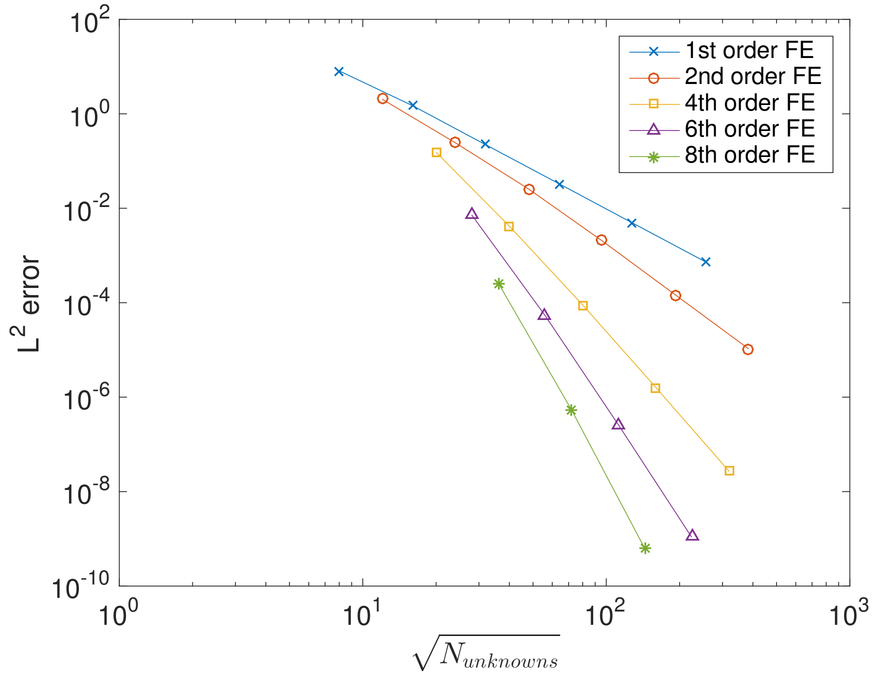

Figure 11: Third order transformed mesh errors as a function of the square root of N_{unknowns}.

Table 10: L^2 norm of the difference between the DGFEM scalar flux and reference solution for given order of finite elements and number of mesh cells for first order orthogonal mesh.

		finite element order				
		1	2	4	6	8
number of mesh cells	16	3.4800	6.1775E-1	2.4481E-2	3.5636E-4	2.6695E-6
	64	7.0630E-1	1.3003E-1	6.3048E-4	1.7471E-6	2.9632E-09
	256	1.1068E-1	1.2167E-2	1.2076E-5	7.6174E-9	3.1213E-12
	1024	1.7186E-2	8.6984E-4	2.0238E-7	3.0997E-11	8.7513E-14
	4096	2.4856E-3	5.7499E-5	3.2576E-9	-	-
	16,384	3.3718E-4	3.7238E-6	-	-	-

Table 11: L^2 norm of the difference between the DGFEM scalar flux and reference solution for given order of finite elements and number mesh cells for first order transformed mesh.

		finite element order				
		1	2	4	6	8
number of mesh cells	16	4.3779	9.7822E-1	4.9514E-2	1.1404E-3	1.5779E-5
	64	1.0636	1.9437E-1	2.1084E-3	1.3649E-5	5.6024E-8
	256	1.8427E-1	2.1919E-2	5.0502E-5	7.7242E-8	7.6887E-11
	1024	2.9440E-2	1.8227E-3	9.3964E-7	3.3367E-10	1.1736E-13
	4096	4.4956E-3	1.3200E-4	1.5960E-8	-	-
	16,384	6.8033E-4	9.4817E-6	-	-	-

Table 12: L^2 norm of the difference between the DGFEM scalar flux and reference solution for given order of finite elements and number of mesh cells for second order transformed mesh.

		finite element order				
		1	2	4	6	8
number of mesh cells	16	8.1134	1.9689	1.2230E-1	4.2791E-3	1.1468E-4
	64	1.4893	2.2841E-1	3.0402E-3	2.6284E-5	1.5938E-7
	256	2.1937E-1	2.4236E-2	6.5709E-5	1.2739E-7	1.8697E-10
	1024	3.2682E-2	1.9632E-3	1.1772E-6	5.4385E-10	-
	4096	4.8375E-3	1.4116E-4	2.0158E-8	-	-
	16,384	7.2294E-4	1.0184E-5	-	-	-

Table 13: L^2 norm of the difference between the DGFEM scalar flux and reference solution for given order of finite elements and number of mesh cells for third order transformed mesh.

		finite element order				
		1	2	4	6	8
number of mesh cells	16	8.1099	2.0451	1.5364E-1	7.2457E-3	2.6153E-4
	64	1.4891	2.4304E-1	4.1710E-3	5.3909E-5	5.3645E-7
	256	2.2057E-1	2.5530E-2	8.9648E-5	2.6223E-7	6.2113E-10
	1024	3.3012E-2	2.0550E-3	1.5906E-6	1.0910E-9	-
	4096	4.8894E-3	1.4711E-4	2.6663E-8	-	-
	16,384	7.2936E-4	1.0551E-5	-	-	-

3.4 Test Problem 4: 1-D Diffusion Limit

The one-dimensional diffusion problem has an exact analytical solution described in Section 2.7. This problem was solved using S_8 level-symmetric angular quadrature, with 8th order finite elements, on an orthogonal spatial grid with periodic boundary conditions on top and bottom to simulate a one-dimensional slab geometry. The left and right boundaries are vacuum. There are 24,300 unknowns on 300 spatial cells. The convergence criteria was $\epsilon_{\text{conv}} = 10^{-12}$ implemented using Equation 39.

The solutions to this problem on the two-dimensional periodic mesh (Figure 36) with $\epsilon = 0.1$, $\epsilon = 0.05$, and $\epsilon = 0.01$ are shown in Figures 12, 13, and 14, respectively. Figure 15 shows lineouts (at $y = 0$) from these two-dimensional solutions to demonstrate the slab geometry solutions. Shown are the analytical solution and three DGFEM solutions ($\epsilon = \{0.1, 0.05, 0.01\}$). The DGFEM solutions trend toward the analytical solution as $\epsilon \to 0$. However, this does not confirm that this code has the diffusion limit or any asymptotic limit. This problem needs to be solved for $\epsilon = 10^{-6}$ to confirm achievement of the diffusion limit but requires a source iteration acceleration. An asymptotic analysis needs to be performed to confirm the discretized transport equation converges to the discretized diffusion equation as $\epsilon \to 0$. This extensive analysis is left to future work but an example of this analysis for the BLD method can be found in Adams [26].

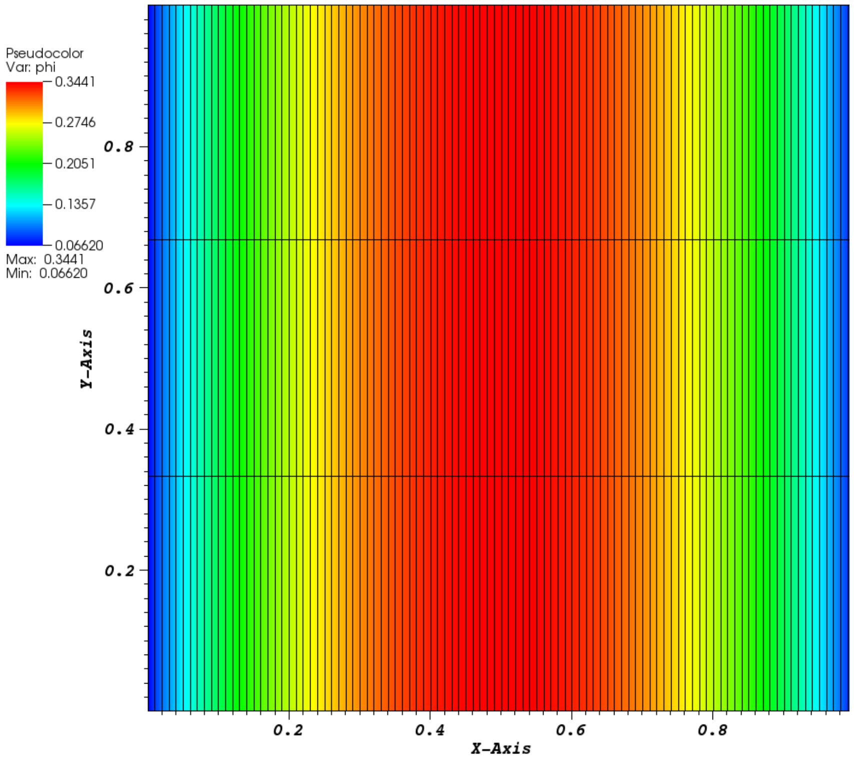

Figure 12: One-dimensional diffusion solution simulated on a two-dimensional mesh using periodic boundaries on top and bottom; mesh shown from Figure 36. Shown is the solution to $\epsilon = 0.1$ of Table 14.

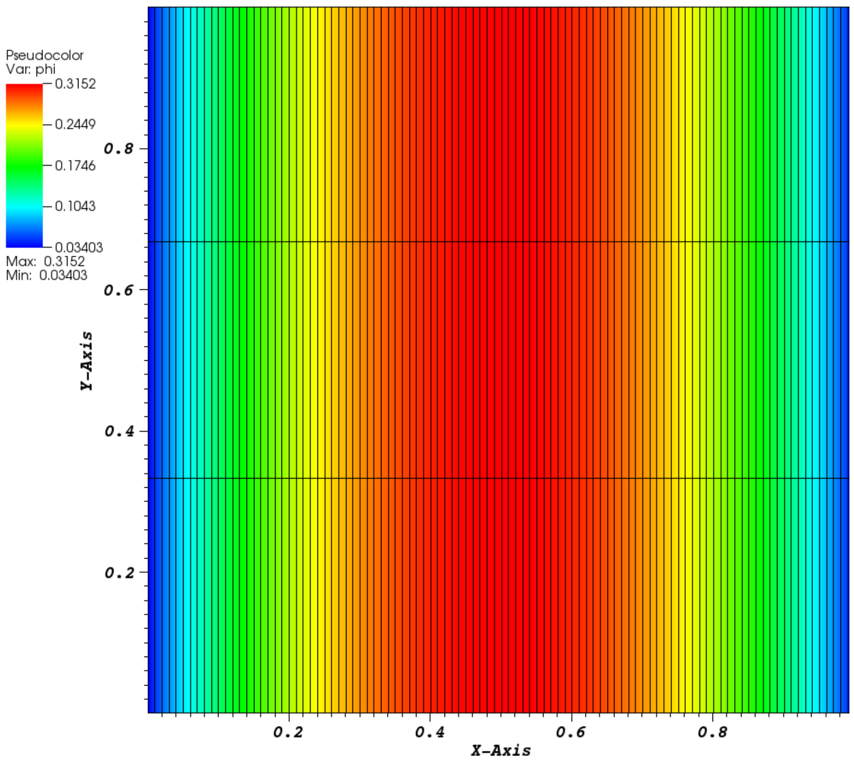

Figure 13: One-dimensional diffusion solution simulated on a two-dimensional mesh using periodic boundaries on top and bottom; mesh shown from Figure 36. Shown is the solution to $\epsilon = 0.05$ of Table 14.

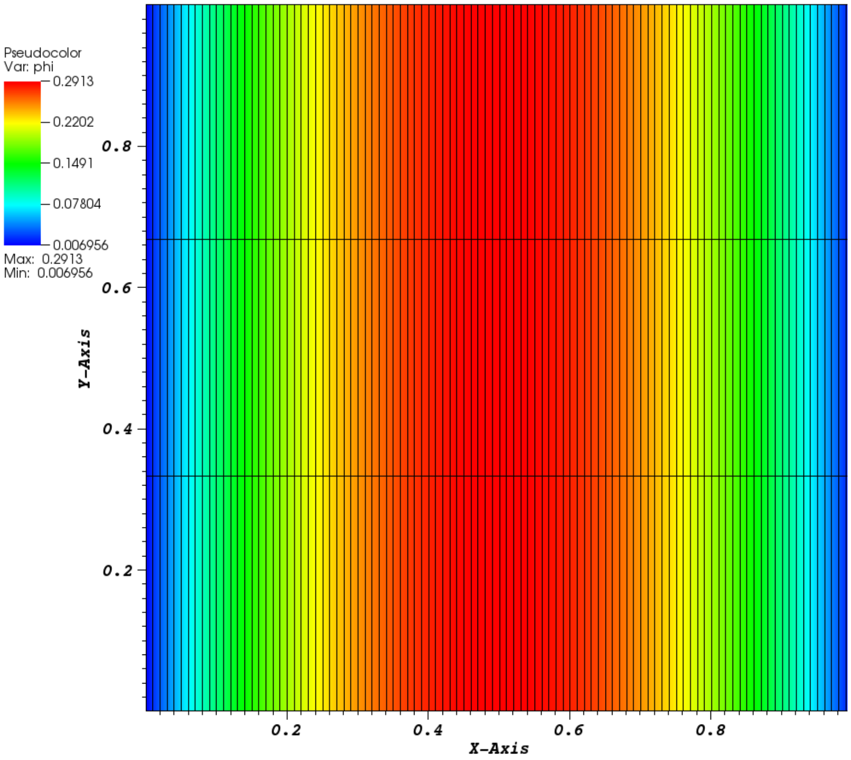

Figure 14: One-dimensional diffusion solution simulated on a two-dimensional mesh using periodic boundaries on top and bottom; mesh shown from Figure 36. Shown is the solution to $\epsilon = 0.01$ of Table 14.

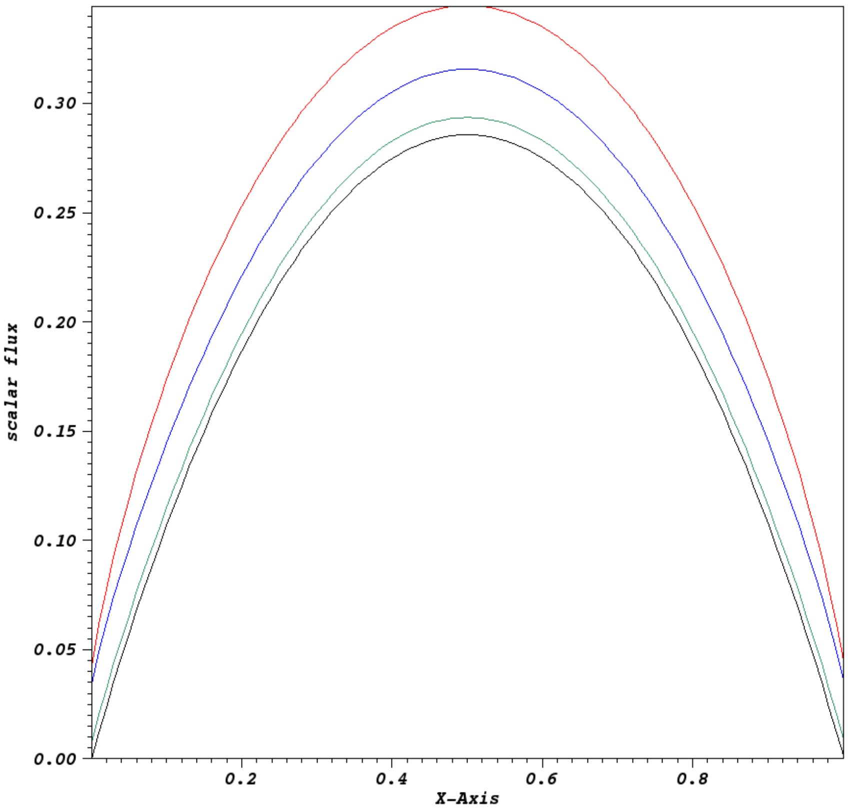

Figure 15: Lineout of solutions (at $y = 0$) from Figures 12 - 14; analytical solution (black) and three DGFEM transport solutions of the one-dimensional diffusion limit problem: $\epsilon = 0.1$ (red), $\epsilon = 0.05$ (blue), and $\epsilon = 0.01$ (green).

Table 14: L^2 errors from the scalar flux of the reference solution and spectral radius of iterations calculated by Equation 38.

ϵ	scattering ratio	spectral radius	L^2 norm
0.1	0.99	0.96	0.066
0.05	0.9975	0.9904	0.036
0.01	0.9999	0.999590	0.0069

3.5 Test Problem 5: 2-D Diffusion Limit

This problem was adapted from Adams [26]. The two-dimensional diffusion problem was solved using S_8 level-symmetric angular quadrature, 8^{th} order finite elements, on a quadrilateral mesh with 8^{th} order polynomial surfaces. All boundaries are vacuum. The solutions are shown in Figures 16 through 18 using the unaccelerated source iteration. There are 20,736 unknowns on 256 spatial zones. The convergence criteria was $\epsilon_{\text{conv}} = 10^{-12}$ implemented using Equation 39.

The L^2 norms of the difference between the DGFEM scalar flux and the reference solution, shown in Table 15, indicate that the DGFEM solution is trending toward the diffusion solution as $\epsilon \to 0$. However, this does not yet confirm that this code has the diffusion limit or any asymptotic limit. This problem needs to be solved for $\epsilon = 10^{-6}$ to confirm achievement of the diffusion limit but requires a source iteration acceleration. An asymptotic analysis needs to be performed to confirm the discretized transport equation converges to the discretized diffusion equation as $\epsilon \to 0$. This extensive analysis is left to future work but an example of this analysis for the BLD method can be found in Adams [26].

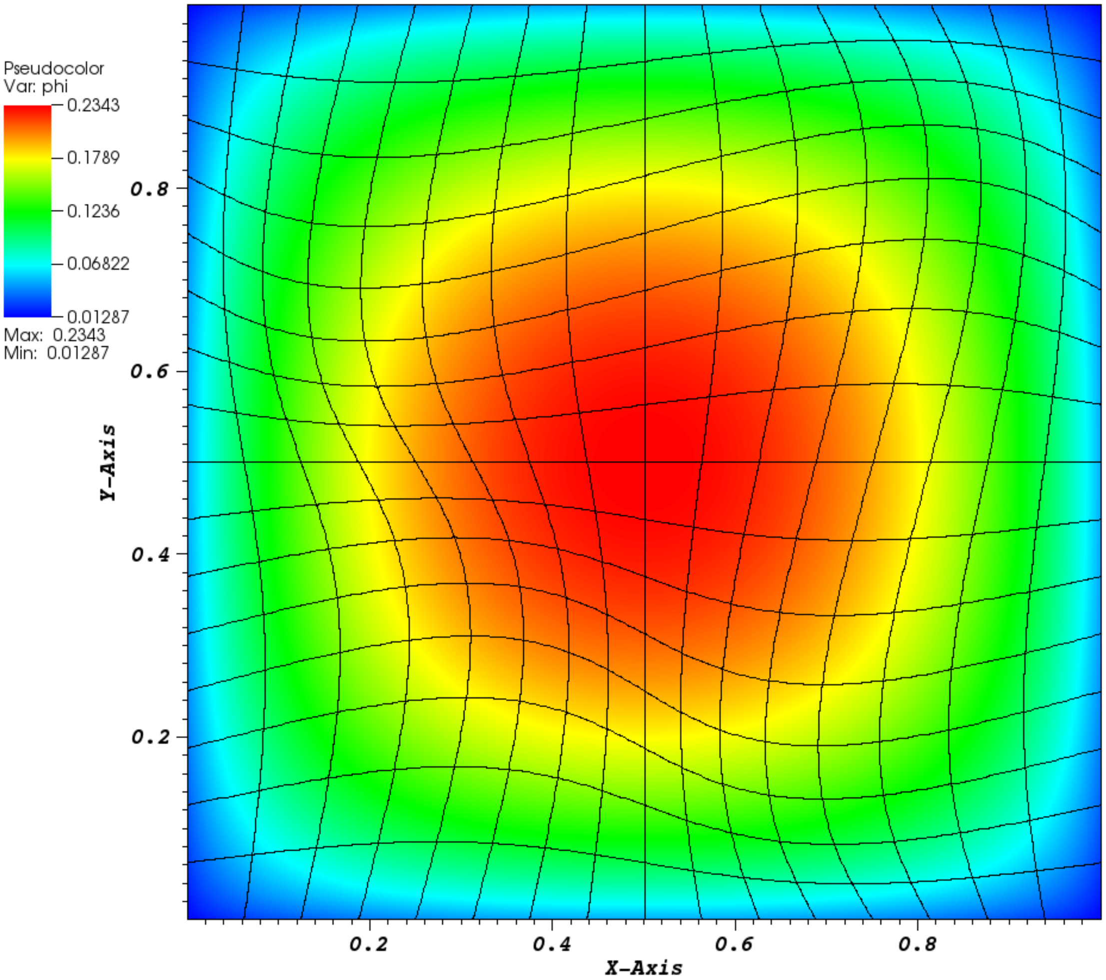

Figure 16: Two-dimensional diffusion problem DGFEM solution for $\epsilon = 0.1$; mesh shown from Figure 37.

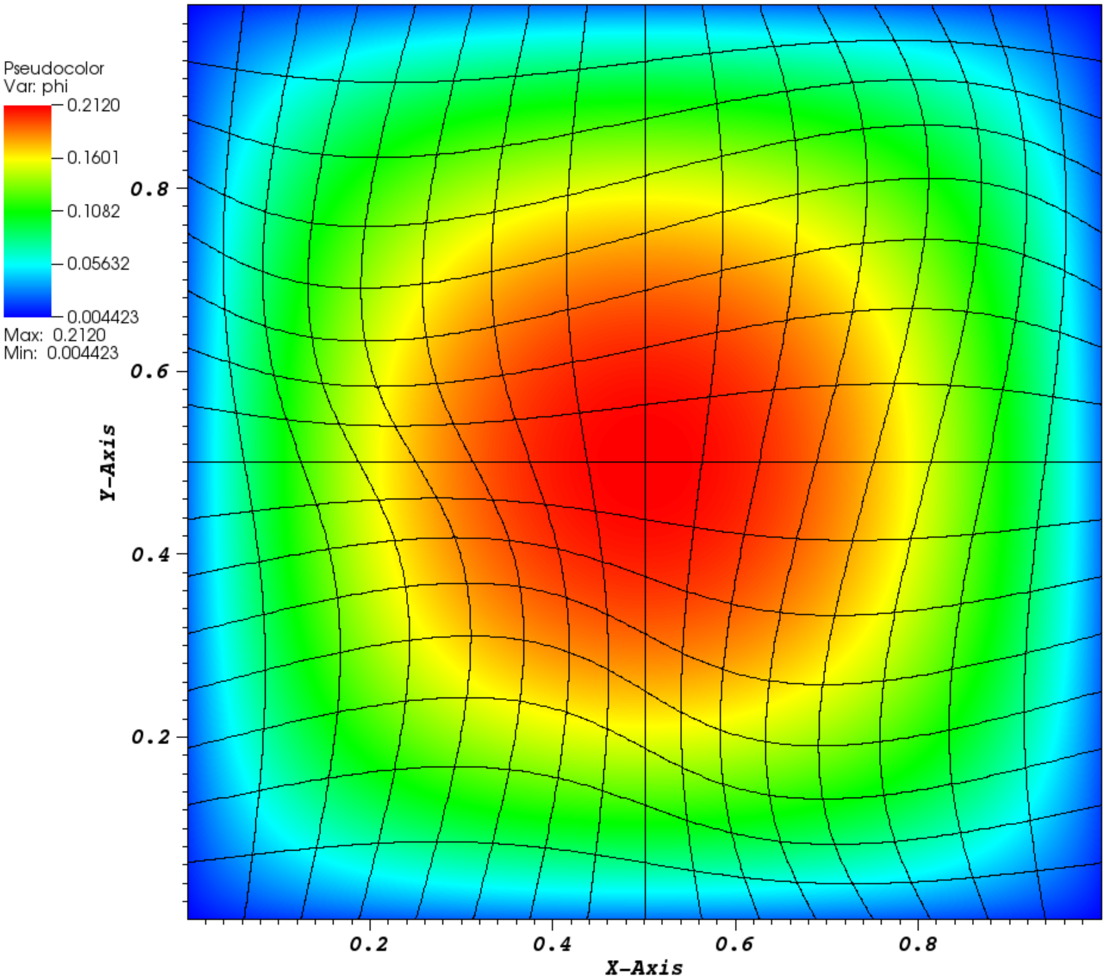

Figure 17: Two-dimensional diffusion problem DGFEM solution for $\epsilon = 0.05$; mesh shown from Figure 37.

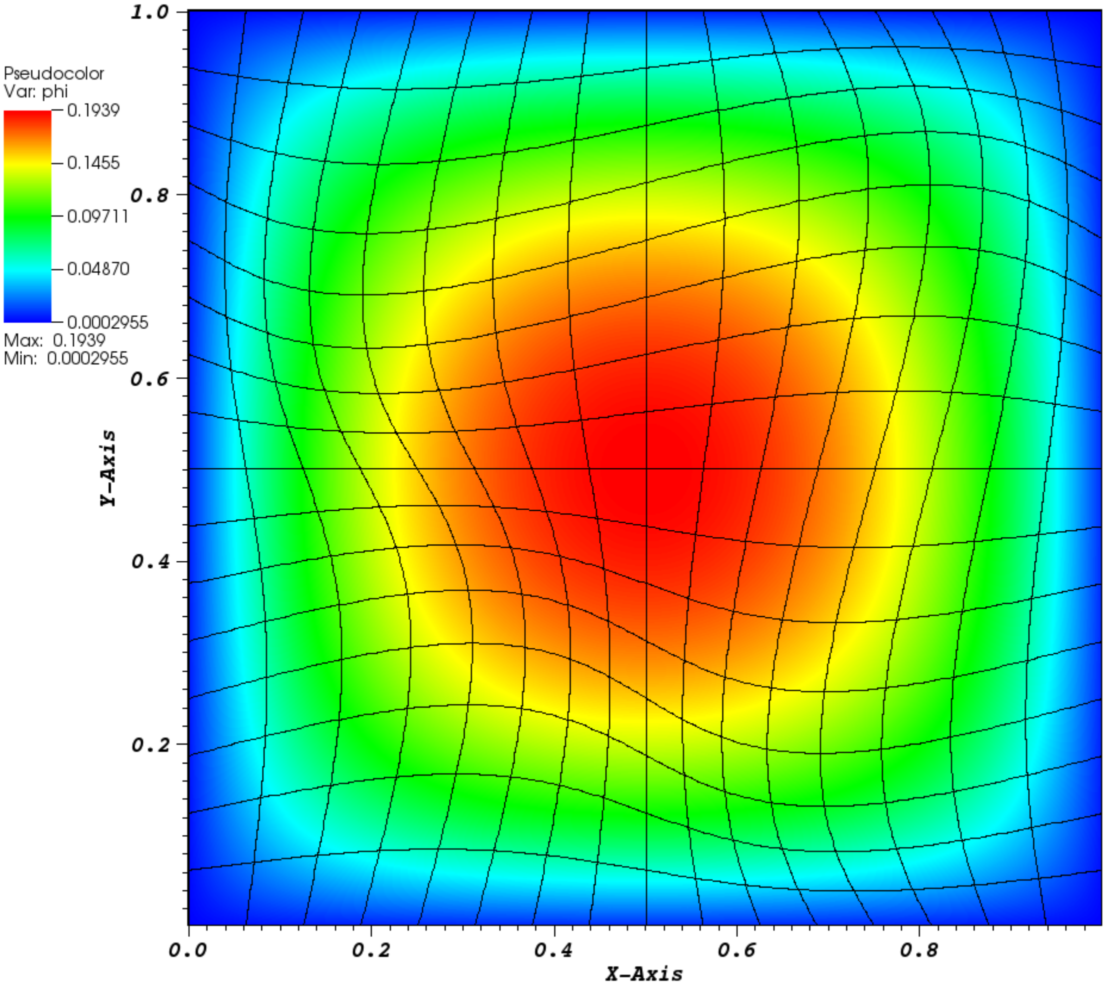

Figure 18: Two-dimensional diffusion problem DGFEM solution for $\epsilon = 0.01$; mesh shown from Figure 37.

Table 15: L^2 norm of the difference between the DGFEM scalar flux solution and the reference solution for several choices of ϵ.

ϵ	scattering ratio $c = 1 - \epsilon^2$	spectral radius (Equation 38)	L^2 norm
0.1	0.99	0.94	0.048
0.05	0.9975	0.9835	0.024
0.01	0.9999	0.99926	0.0048

3.6 Test Problem 6: Strong Scatter with Discontinuous Boundary Conditions

The problem description is in Section 2.7.6. Figure 19 shows the DGFEM calculation of the scalar fluxes. The white space shows where the scalar flux is negative. Figure 20 shows the same data on a log scale. The solution is smooth (except where the solution is negative) and changes over 22 orders of magnitude. That is, the polynomial basis functions smoothly model the exponential behavior in this problem. On orthogonal meshes in cylindrical geometry, Palmer [58] numerically demonstrates three methods that have results similar to Figures 19 and 20 (bilinear discontinuous FEM (BLD), mass-lumped BLD (MLBLD), and surface-lumped BLD (SLBLD)), and two methods that are positive and smooth (fully-lumped BLD (FLBLD) and simple corner balance (SCB)). Numerical results from Adams [22] also show negative fluxes using the MLBLD and BLD methods in Cartesian geometry. Adams [26] states that anisotropic fluxes incident on unresolved boundaries cause issues within the interior of the solution and lumping can improve the solution behavior. The solution here used S_4 level-symmetric quadrature, 8th-order finite elements, and no lumping technique. The spectral radius was 0.999 (by Equation 38), demonstrating a slow convergence rate.

In the context of radiation hydrodynamics, negative fluxes imply negative energies. The equations of state can produce negative temperatures, negative densities, and negative pressures, which are non-physical. It will be important that the radiation transport method properly handles these negative flux regions to prevent errors in the equations of state.

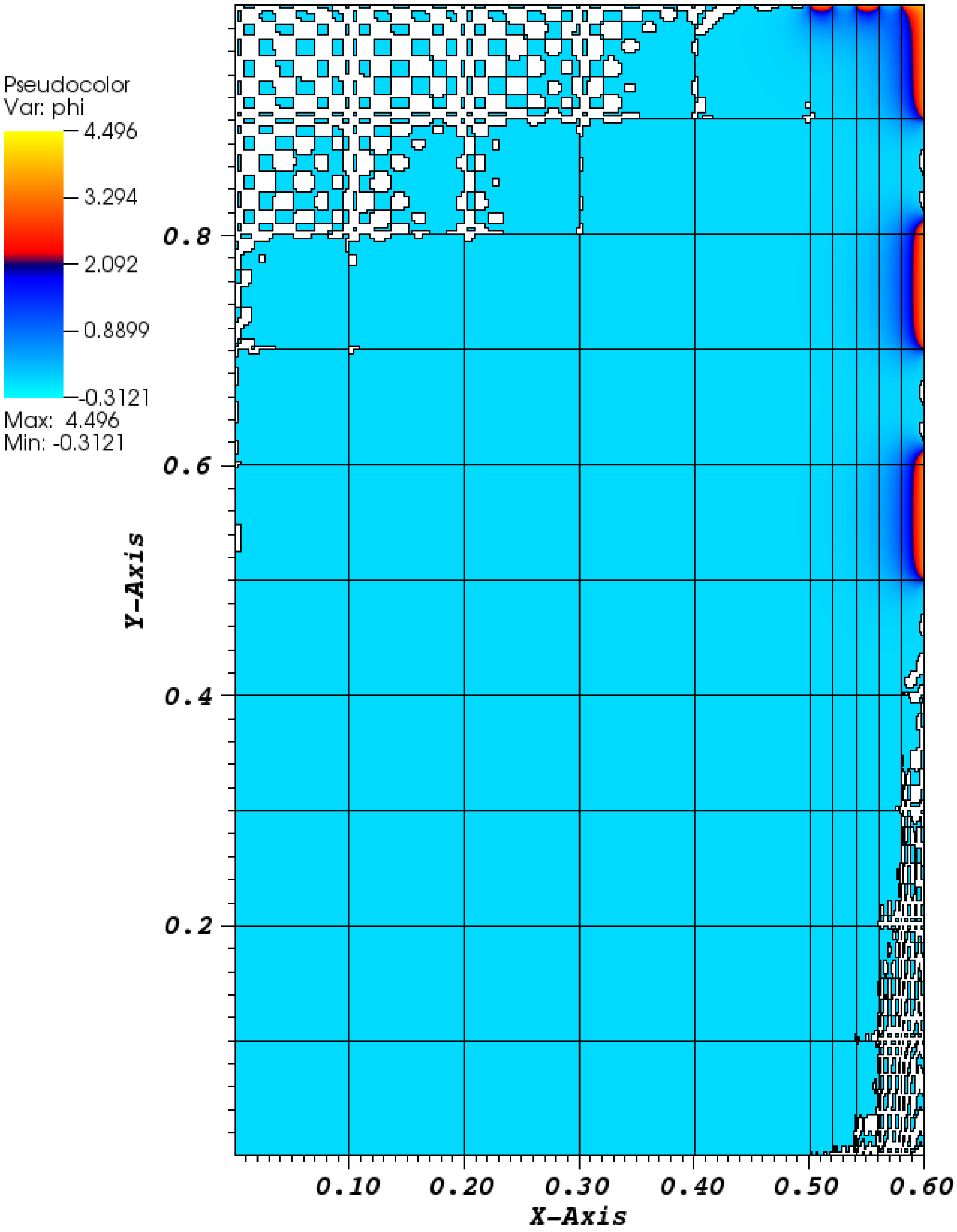

Figure 19: Test Problem 6: Optically Thick Problem A scalar flux; white space shows where solution is negative; mesh shown from Figure 38.

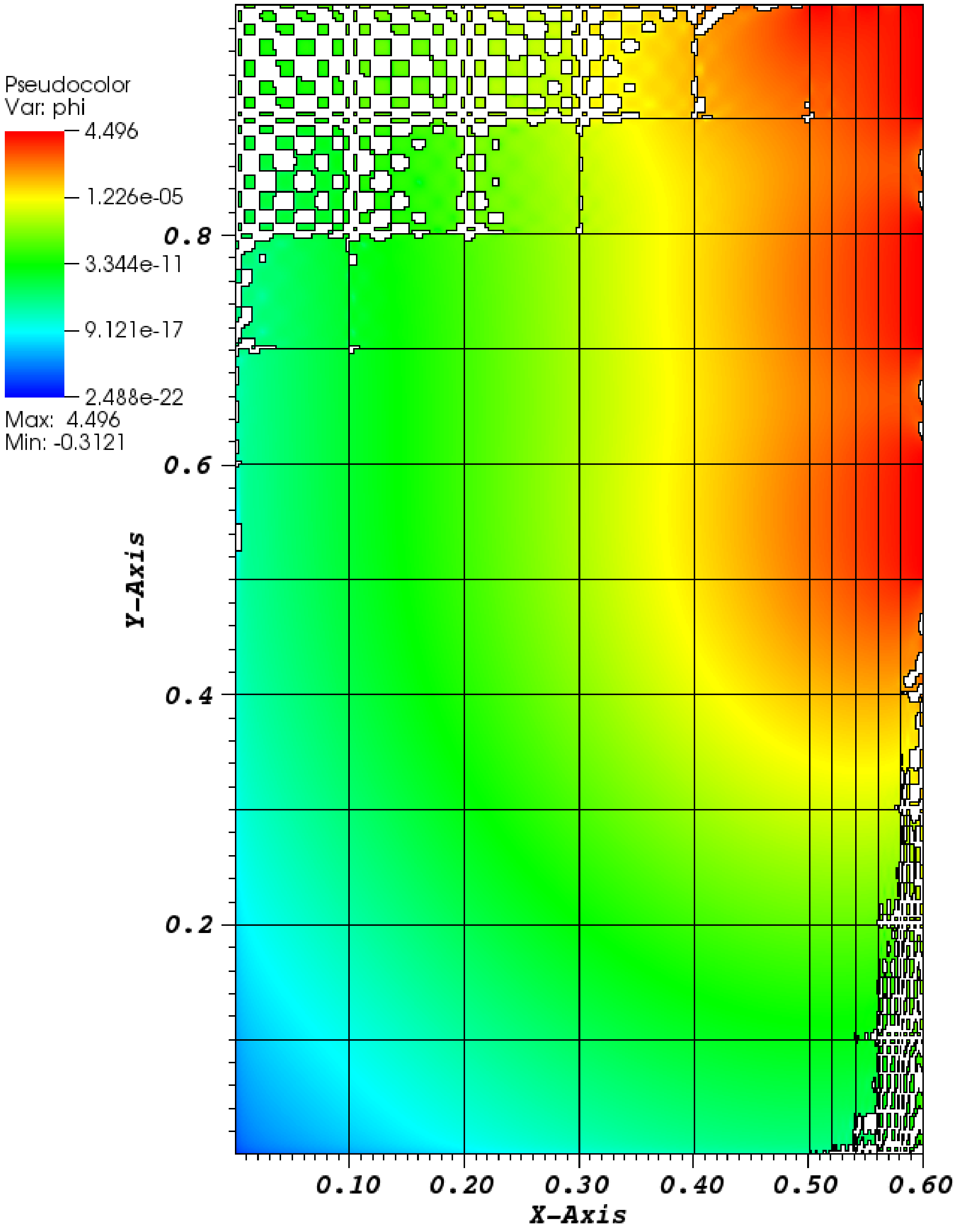

Figure 20: Test Problem 6: Optically Thick Problem A scalar flux on a log scale; white space indicates where solution is negative; mesh shown from Figure 38.

3.7 Test Problem 7: Material Discontinuity Stress Test

This problem is described in Section 2.7.7. The resulting DGFEM scalar flux solution is shown in Figure 21. The white space shows where the scalar flux is negative. Figure 22 is the same solution on a logarithmic scale. The solution is relatively smooth (except where the solution is negative) and changes over 14 orders of magnitude. The solution was computed with S_4 level-symmetric quadrature, with 8th order finite elements, and no lumping techniques were used. On orthogonal meshes in cylindrical geometry, Palmer [58] numerically demonstrates two methods that have similar results to Figures 21 and 22 (BLD and MLBLD) and two methods that are positive and smooth (FLBLD and SCB). The spectral radius was 0.99999 (by Equation 38), demonstrating a very slow convergence rate.

The majority of the negative fluxes appear in the very thick absorbing region where oscillations are apparent. There are slightly visible oscillations in the unrefined boundary layers of the scattering region but they do not go negative. Also seen are some ray effects.

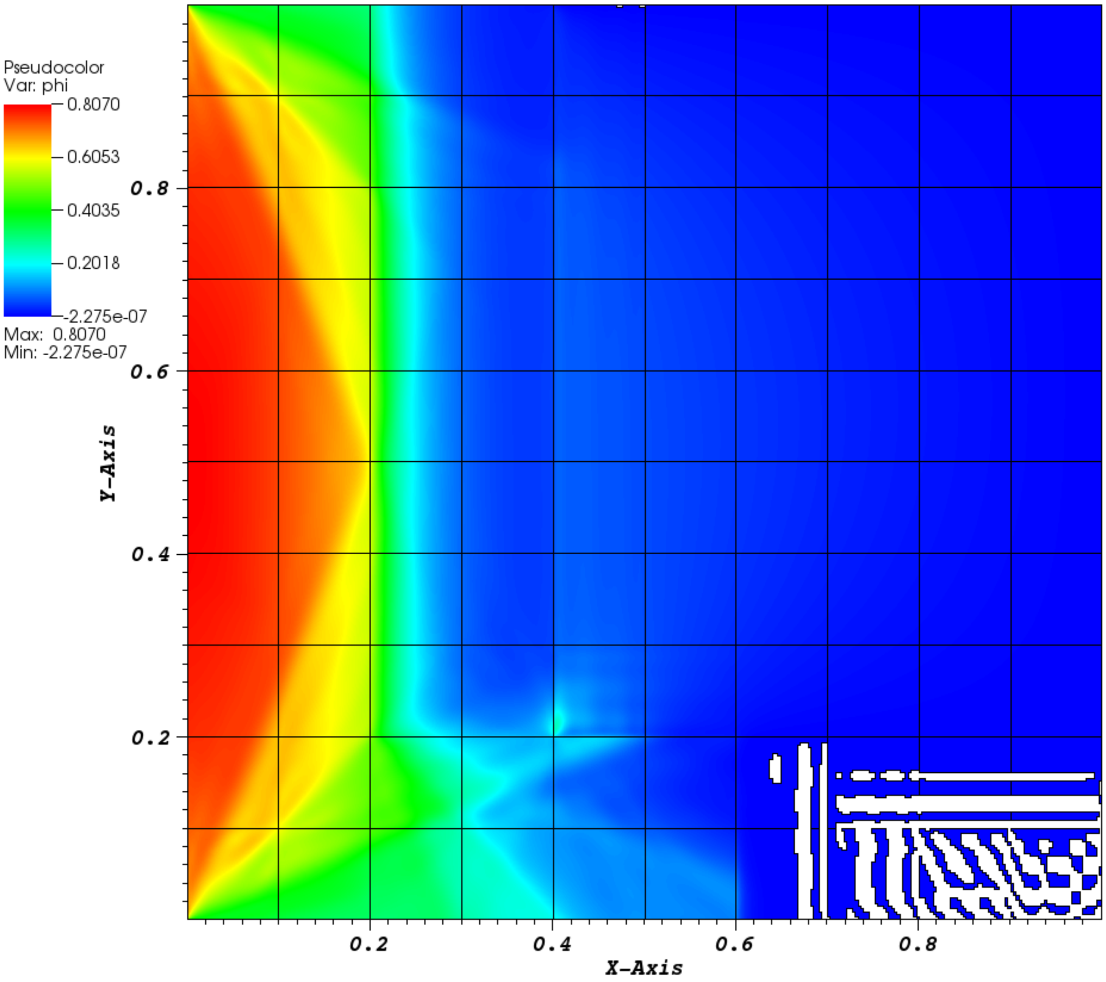

Figure 21: Test Problem 7 scalar flux; white space shows where solution is negative; mesh shown from Figure 39.

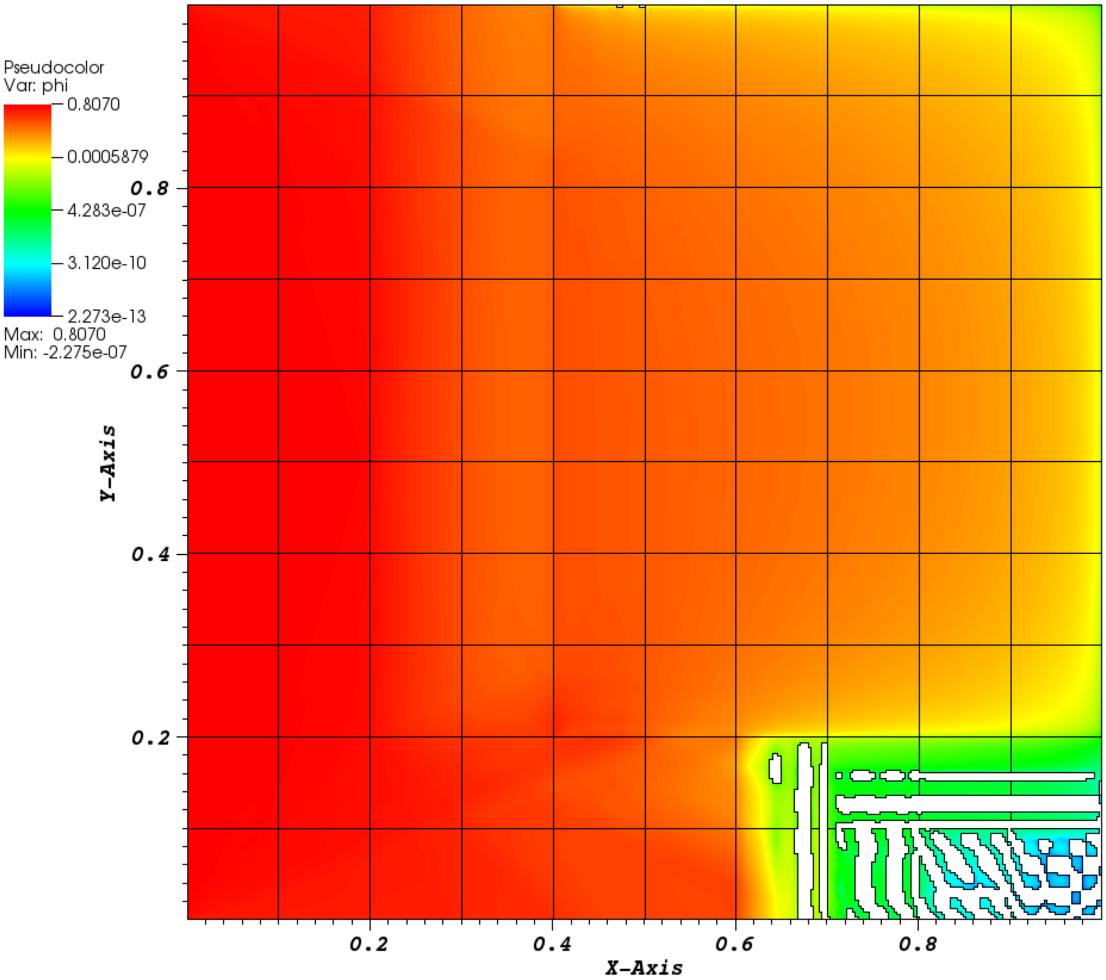

Figure 22: Test Problem 7 scalar flux on a log scale; white space indicates where solution is negative; mesh shown from Figure 39.

3.8 Test Problem 8: 2-D Diffusion Limit Direct Solve Method

This is the same diffusion limit problem as in Test Problem 5 but using the direct solve method. The computational time is significant for problems with a large number of unknowns (e.g. on the order of 10^5), so this problem was limited to 4th order finite elements whereas 8th order was used in Test Problem 5. S_4 level-symmetric quadrature was used on a second order mesh (Figure 40). There are 1600 unknowns in 64 spatial cells. The solution is shown in Figure 23. The result demonstrates that this solution method may be a viable alternative to source iteration especially in optically thick problems when there are relatively few unknowns.

An issue arises when solving this linear system with a direct solve. The operator matrix has an increasing condition number with increasing scattering ratio (Figure 24), causing the solve to break down beyond $\epsilon = 0.0005$. The condition number,

$$\kappa = \|A\| \|A^{-1}\| \tag{78}$$

is an indication of how sensitive the solution is to small perturbations in the linear algebra problem.

Table 16: L^2 norms of the difference between the DGFEM scalar flux and the reference solution for several choices of ϵ.

ϵ	scattering ratio	L^2 norm
0.1	0.99	0.04654713
0.05	0.9975	0.023714251
0.01	0.9999	0.0048038978
0.005	0.999975	0.0024034884
0.001	0.999999	0.00048896782
0.0005	0.99999975	0.00027587357
0.0001	0.99999999	0.040468175

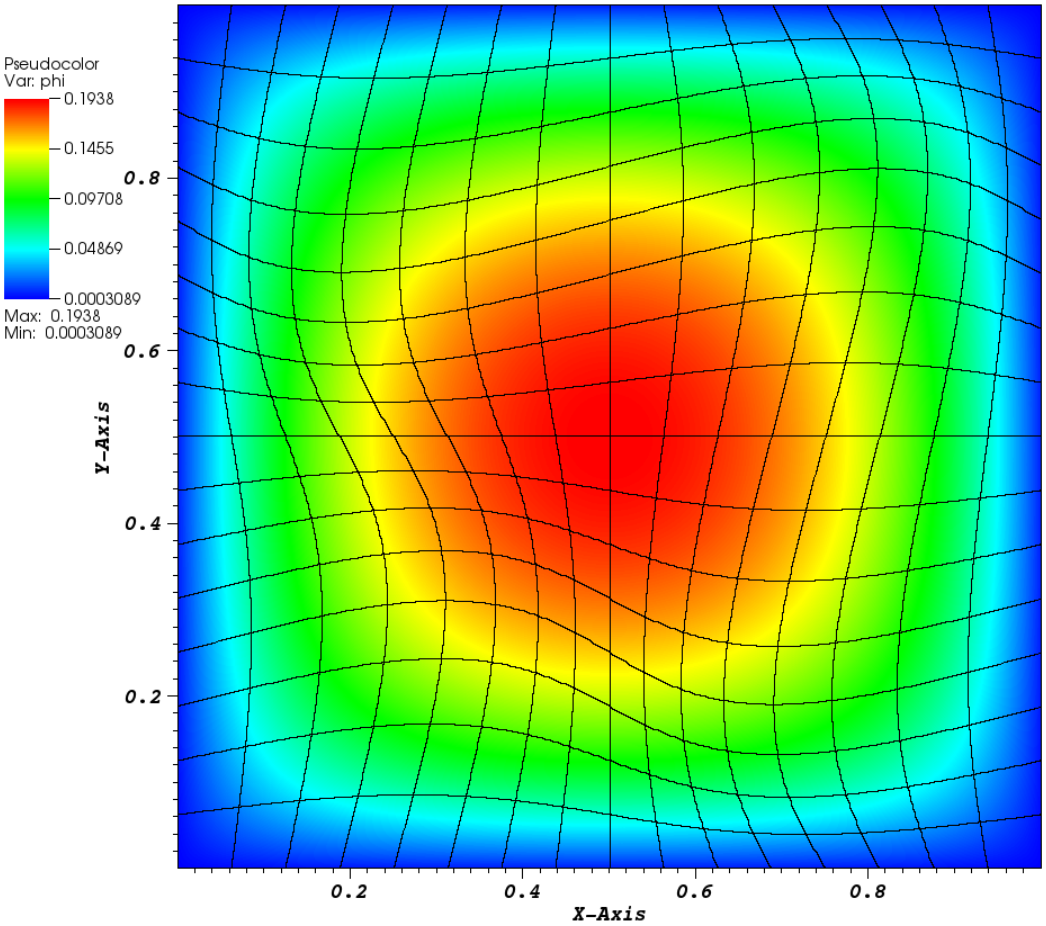

Figure 23: Test problem 8: 2-D diffusion limit problem solved with direct solve method; mesh shown from Figure 40.

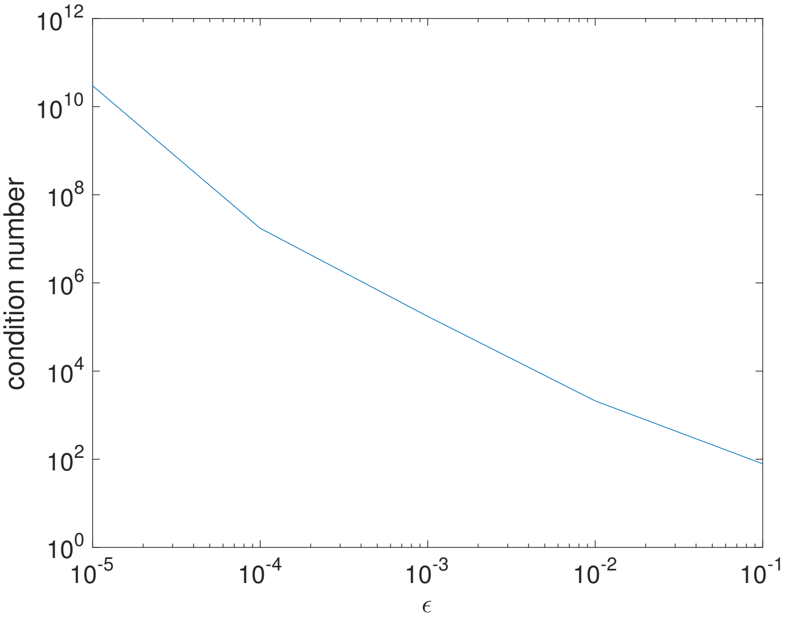

Figure 24: Condition number of the large matrix as a function of ϵ.

4 Conclusions

The objectives of this research were to develop and characterize a radiation transport code using high order finite elements in optically thick material on spatial grids with curved surfaces. Employing the general finite element library, MFEM, several test problems were solved to characterize the solver and serve as a proof-of-concept.

This research found it important to numerically integrate each of the finite element terms consistently. Specifically, the quadrature order that is used for the integrations should be equal. Presently, the integration orders of each term were set to the maximum of the default integration orders for a given problem. The cost involved is in spending computational time integrating functions to a higher order than is necessary. While this research was not directly concerned with optimizing computational time, this issue could be better resolved.

The uniform infinite medium test problem was successfully solved demonstrating early viability of the transport solver. Given cross-sections, a fixed source, incident fluxes on the boundaries, and pre-generated level-symmetric quadrature sets, MFEM generates a system of equations to solve for the angular flux. A direct-solve linear algebra solver was used to solve these equations for the angular flux. The scalar flux was calculated by summing the weighted angular fluxes and used in the scattering source term for the next iteration. This source iteration was repeated until a convergence criteria was satisfied and the final scalar flux was output to VisIt for visualization. The analytic solution was achieved in this test problem indicating that the aforementioned algorithm was implemented correctly.

The Reed-Hill problem tested the ability to model spatially dependent cross-sections and fixed sources. The solution indicates this methodology can model material interfaces with strong changes in material properties that result in sharp changes in the flux profile. With sufficient spatial mesh refinement, the high order finite elements model the sharp flux changes without significant oscillation at these material interfaces. However, some oscillation was observed on the coarser mesh although they do not go negative. In lieu of a reflecting boundary condition, the problem was modeled reflected across this boundary to achieve the desired behavior at the reflecting location.

Performing a convergence study resulted in various convergence rates with respect to the square root of the number of unknowns. In all cases, increasing the number of unknowns (either by increasing the finite element order and/or refining the mesh) reduced the error. The convergence rates are approximately $p+1$, where p is the finite element order, similar to the results found in Wang and Ragusa [34]. It is apparent that the convergence rates are fairly insensitive to the degree of curvature in the edges of the mesh.

Solving the homogeneous optically thick problems showed this method trends toward the analytical one-dimensional diffusion solutions using high order finite elements on a fine orthogonal spatial grid. Similarly, the results showed the two-dimensional transport solution trending toward the diffusion equation solution. The confirmation that this code has the diffusion limit cannot be achieved until it successfully solves these problem for $\epsilon = 10^{-6}$. These high scattering ratio calculations took longer than is practical so research in optically thick materials is limited until a synthetic acceleration is properly implemented. Both the one- and two-dimensional solutions demonstrated first-order convergence with respect to the smallness factor ϵ. The analytical diffusion limit analysis has $O\left(\epsilon^2\right)$ convergence. This implies the arise of a $O\left(\epsilon\right)$ term in the discretized transport equation. This analysis is left to future work.

Test Problem 6 revealed non-physical negative fluxes in the boundary layer of the interior solution. Sufficiently far from the boundary layer, the solution is smoothly modeled. These negative fluxes was expected from other research and have been investigated to correct these negative fluxes. Maginot [36] and Maginot et al. [35, 41] have researched lumping techniques with high order finite elements and have determined that lumping alone may not preserve a positive solution.

Test Problem 7 specifically exposed the difficult task of modeling optically thick and thin regions simultaneously. Since this phenomenon naturally arises in thermal radiation transport problems, it is important to consider throughout the method development. Negative fluxes appear in the absorption region and a relatively smooth positive solution appears elsewhere. This problem also tested the boundary layers of the scattering region where the incident flux was anisotropic. These regions can be sensitive to anisotropic fluxes and some oscillation was present although the solution stayed positive. It is conceivable that implementing a lumping technique would dampen the oscillations and make those areas less susceptible to negative fluxes by making the method more local. However, making the method more local could have a negative effect on the optically thin regions where the mean free path is much greater.

The direct solve method showed promise in the ability to model optically thick problems without having to iterate upon a slowly converging scattering source. However, as ϵ was driven toward zero the large matrix became increasingly ill-conditioned. Small changes in the input caused increasingly larger changes in the solution, including any associated error. This caused the solution to rapidly diverge from the diffusion equation solution. For well-conditioned problems (e.g. larger values of ϵ), the direct solve method solved the solution as accurately as the source iteration method. Since the direct solve matrix size is sensitive to the number of unknowns and angular quadrature order, there is a practical limitation on the size of the solvable problem.

4.1 Future Work

Although implementing synthetic acceleration for the source iteration was not a specific goal for this research, we did make an attempt to implement it from Wang and Ragusa [20] but the implementation required significant modification to the MFEM source code. This implementation will be necessary for future work in the diffusion limit.

The method of manufactured solutions was used for a convergence study. An extensive use of this method will include exercising each of the terms in the transport equation to reveal any errors within the code. This is done by sequentially adjusting the magnitude of each term of the transport equation independently [59].

In the future, the ability to model reflecting boundaries would be beneficial in comparing results form this method with analytic results and in code-to-code comparisons. The work presented in this research used a combination of periodic boundaries, fixed incident isotropic angular fluxes, and modeling the reflected problem across the reflected boundary condition. While these were sufficient for the test problems here, this approach may not be adequate in the future. Additionally, it would be advantageous to be able to test simple problems that utilize periodic boundaries in alignment with the goals of this research. Specifically, the process to transform a mesh to have curved edges does not work with meshes with periodic boundaries or meshes not on the unit square. It could be instructive to perform the Reed-Hill and one-dimensional diffusion problems on meshes with curved surfaces and also allowing for additional test problems.

MFEM can be compiled and used to compute each spatial cell in parallel. This technique was not evaluated in our research, but it could be implemented in a future investigation. The computational time is likely to decrease dramatically as there were over 1000 spatial cells in some test problems described above.

Eventually, this radiation transport code could be used in conjunction with a hydrodynamics code to simulate radiation hydrodynamics problems. Much work needs to be done to characterize and optimize this radiation transport code in the various physical regimes achievable in high energy density physics problems. Other material dependent interactions need to be added to the code. Adding a material temperature dependency turns the system of equations into a non-linear problem, further increasing the complexity of the solve. Hence, it is important to robustly and accurately solve the linear transport equations prior to adding these non-linear terms.

References

[1] R. Paul Drake. High-energy-density physics. *Physics Today*, 63(3):8–9, June 2010.

[2] Veselin A. Dobrev, Tzanio V. Kolev, and Robert N. Rieben. High-order curvilinear finite element methods for Lagrangian hydrodynamics. *SIAM Journal of Scientific Computing*, 34(5):B606 – B641, 2012.

[3] MFEM: Modular finite element methods. `mfem.org`, 2015.

[4] John Castor. *Radiation Hyrdodynamics*. Cambridge, 2007.

[5] Jeffery D. Densmore and Edward W. Larsen. Asymptotic equaillibrium diffusion analysis of time-dependent Monte Carlo methods for grey radiative transfer. *Journal of Computational Physics*, 199:175–204, 2004.

[6] B. L. Kirk. Overview of Monte Carlo radiation transport codes. *Radiation Measurements*, 45:1318–1322, 2010.

[7] W. H. Reed and T. R. Hill. Triangular mesh methods for the neutron transport equation. Technical Report LA-UR-73-479, Los Alamos National Laboratory, 1973.

[8] P. Lasaint and P. A. Raviart. On a finite element method for solving the neutron transport equation. In Carl de Boor, editor, *Mathematical Aspects of Finite Elements in Partial Differential Equations*, pages 89–123. Academic Press, 1974.

[9] W. H. Reed, T. R. Hill, F. W. Brinkley, and K. D. Lathrop. TRIPLET: A two-dimensional multigroup, triangular-mesh, planar geometry, explicit transport code. Technical report, Los Alamos National Laboratory, 1973.

[10] T. J. Seed, Jr. W. F. Miller, and G. E. Bosler. TRIDENT: A new triangular mesh discrete-ordinates code. Technical report, University of California, Los Alamos Scientific Laboratory, 1978.

[11] T. J. Seed, W. F. Miller, Jr., and F. W. Brinkley, Jr. TRIDENT: A two-dimensional, multigroup, triangular mesh discrete ordinates, explicit neutron transport code. Technical Report LA-6735-M, Los Alamos National Laboratory, March 1977.

[12] Ron T. Ackroyd. *Finite Element Methods for Particle Transport: Application to Reactor and Radiation Physics.* John Wiley & Sons Inc., 1997.

[13] Maurice Mordant. Some efficient Lagrangian mesh finite elements encoded in ZEPHYR for two-dimensional transport calculations. *Annals of Nuclear Energy*, 8:657–675, 1981.

[14] Claes Johnson and Juhani Pitkaranta. Convergence of a fully discrete scheme for two-dimensional neutron transport. *SIAM Journal of Numerical Analysis*, 20(5):951–966, 1983.

[15] Mohammad Asadzadeh. Analysis of a fully discrete scheme for neutron transport in two-dimensional geometry. *SIAM Journal of Numerical Analysis*, 23(3):543–561, 1986.

[16] Edward W. Larsen, J. E. Morel, and J. Warren F. Miller. Asymptotic solutions of numerical transport problems in optically thick, diffusive regimes. *Journal of Computational Physics*, 1987.

[17] Edward W. Larsen and J. E. Morel. Asymptotic solutions of numerical transport problems in optically thick, diffusive regimes II. *Journal of Computational Physics*, 83:212–236, 1989.

[18] Edward W. Larsen. The asymptotic diffusion limit of discretized transport problems. *Nuclear Science and Engineering*, 112:336–346, 1992.

[19] Marvin L. Adams and William R. Martin. Diffusion synthetic acceleration of discontinuous finite element transport iterations. *Nuclear Science and Engineering*, 111:145–167, 1992.

[20] Yaqi Wang and Jean C. Ragusa. Diffusion synthetic acceleration for high-order discontinuous finite element S$_N$ transport schemes and application to locally refined unstructured meshes. *Nuclear Science and Engineering*, 166:145–166, 2010.

[21] Christoph Börgers, Edward W. Larsen, and Marvin L. Adams. The asymptotic diffusion limit of a linear discontinuous discretization of a two-dimensional linear transport equation. *Journal of Computational Physics*, 98(2):285–300, 1992.

[22] Marvin L. Adams. Discontinuous finite-element transport solutions in the thick diffusion limit in Cartesian geometry. *The American Nuclear Society International Topical Meeting*, 1991.

[23] Todd S. Palmer and Marvin L. Adams. Curvilinear geometry transport discretization in the "thick" diffusion limit. *Proceedings of the International Conference Math. Methods & Supercomputing in Nuc. Appl.*, 1993.

[24] Todd A. Wareing, John M. McGhee, and Jim E. Morel. ATTILA: A three-dimensional, unstructured tetrahedral mesh discrete ordinates transport code. *Transactions of the American Nuclear Society*, 75:146–147, 1996.

[25] J. M. McGhee and T.A. Wareing. *Attila Version 2: User's Manual.* Los Alamos National Laboratory, 2000.

[26] Marvin L. Adams. Discontinuous finite element transport solutions in thick diffusive problems. *Nuclear Science and Engineering*, 137(3):298–333, 2001.

[27] Hiromi G. Stone and Marvin L. Adams. A piecewise linear finite element basis with application to particle transport. *Nuclear Mathematical and Computational Sciences: A Century in Review, A Century Anew*, 2003.

[28] Teresa S. Bailey, Marvin L. Adams, Jae H. Chang, and James S. Warsa. A piecewise linear discontinuous finite element spatial discretization of the transport equation in 2D cylindrical geometry. *International Conference on Mathematics, Computational Methods & Reactor Physics*, 2009.

[29] T. S. Bailey, J. H. Chang, J. S. Warsa, and M. L. Adams. A piecewise bi-linear discontinuous finite element spatial discretization of the S_N transport equation. *International Conference on Mathematics and Computational Methods Applied to Nuclear Science and Engineering*, 2011.

[30] J. E. Morel and J. S. Warsa. A lumped bilinear-discontinuous S_N spatial discretization for r-z quadrilateral meshes. *Transactions of the American Nuclear Society*, 95:873, 2006.

[31] Jim E. Morel, Alejandro Gonzales-Aller, and James S. Warsa. A lumped linear-discontinuous spatial discretization scheme for triangular-mesh S_N calculations in r-z geometry. *Nuclear Science and Engineering*, 155:168–178, 2007.

[32] Jim E. Morel and James S. Warsa. An S_N spatial discretization scheme for tetrahedral meshes. *Nuclear Science and Engineering*, 151:157–166, 2005.

[33] Yaqi Wang and Jean C. Ragusa. On the convergence of DGFEM applied to the discrete ordinates transport equation for structured and unstructured triangular meshes. *Nuclear Science and Engineering*, 163:56–72, 2009.

[34] Yaqi Wang and Jean C. Ragusa. A high-order discontinuous Galerkin method for the S_N transport equations on 2D unstructured triangular meshes. *Annals of Nuclear Energy*, 36:931–939, 2009.

[35] Peter G. Maginot, Jean C. Ragusa, and Jim E. Morel. Characterization of high order spatial discretizations and lumping techniques for disontinuous finite element S_N transport. *M&C 2013*, pages 2327–2338, May 2013.

[36] Peter Maginot. *Higher Order Discontinuous Finite Element Methods for Discrete Ordinates Thermal Radiative Transfer.* PhD thesis, Texas A&M University, 2015.

[37] Yaqi Wang. *Adaptive Mesh Refinement Solution Techniques for the Multigroup S_N Transport Equation Using a Higher-Order Discontinuous Finite Element Method*. PhD thesis, Texas A&M University, 2009.

[38] Philip M. Gresho and Robert L. Lee. Don't suppress the wiggles — they're telling you something! *Computers & Fluids*, 9:223–253, 1981.

[39] Steven Hamilton, Michele Benzi, and Jim Warsa. Negative flux fixups in discontinuous finite element S_N transport. *International Conference on Mathematics, Computational Methods & Reactor Physics*, May 2009.

[40] Peter G. Maginot, Jim E. Morel, and Jean C. Ragusa. A non-negative moment-preserving spatial discretization scheme for the linearized Boltzmann transport equation in 1-D and 2-D Cartesian geometries. *Journal of Computational Physics*, 231:6801–6826, 2012.

[41] Peter G. Maginot, Jean C. Ragusa, and Jim E. Morel. Lumping techniques for DFEM S_N transport in slab geometry. *Nuclear Science and Engineering*, 2015.

[42] Thomas A. Brunner. Preserving positivity of solutions to the diffusion equation for higher-order finite elements in under resolved regions. In *ANS M&C - Joint International Conference on Mathematics and Computation (M&C), Supercomputing in Nuclear Applications (SNA) and the Monte Carlo (MC) Method*, April 2015.

[43] J. C. Ragusa, J. L. Guermond, and G. Kanschat. A robust S_N-DG-approximation for radiation transport in optically thick and diffusive regimes. *Journal of Computational Physics*, 231(4):1947 – 1962, February 2012.

[44] Teresa Bailey. Personal communication, 2015.

[45] Cheuk Lau. Personal communication, 2015.

[46] Peter G. Maginot. Personal communication, 2016.

[47] K. D. Lathrop and B. G. Carlson. Discrete ordinates angular quadrature of the neutron transport equation. Technical report, Los Alamos Scientific Laboratory of the University of California, 1965.

[48] E. E. Lewis and W. F. Miller, Jr. *Computational Methods of Neutron Transport*. American Nuclear Society, 1993.

[49] Todd A. Wareing, John M. McGhee, Jim E. Morel, and Shawn D. Pautz. Discontinuous finite element S_N methods on three-dimensional unstructured grids. *Nuclear Science and Engineering*, 138:256–268, 2001.

[50] Timothy A. Davis. *Direct Methods for Sparse Linear Systems*. Society for Industrial and Applied Mathematics, 2006.

[51] Timothy A. Davis. Algorithm 832: Umfpack v4.3 — an unsymmetric-pattern multifrontal method. *ACM Transactions on Mathematical Software*, 30(2):196–199, June 2004.

[52] Hank Childs, Eric Brugger, Brad Whitlock, Jeremy Meredith, Sean Ahern, David Pugmire, Kathleen Biagas, Mark Miller, Cyrus Harrison, Gunther H. Weber, Hari Krishnan, Thomas Fogal, Allen Sanderson, Christoph Garth, E. Wes Bethel, David Camp, Oliver Rübel, Marc Durant, Jean M. Favre, and Paulr Navrátil. Visit: An end-user tool for visualizing and analyzing very large data. In *High Performance Visualization–Enabling Extreme-Scale Scientific Insight*, pages 357–372. Oct 2012.

[53] Marvin L. Adams and Edward W. Larsen. Fast iterative methods for discrete-ordinates particle transport calculations. *Progress in Nuclear Energy*, 40(1):3–159, 2002.

[54] F. Malgavi and G. C. Pomraning. Initial and boundary conditions for diffusive linear transport problems. *Journal of Mathematical Physics*, 32, 1990.

[55] William H. Reed. New difference schemes for the neutron transport equation. *Nuclear Science and Engineering*, 46(2):309–314, 1971.

[56] Ryan G. McClarren. *Spherical Harmonics Methods for Thermal Radiation Transport*. PhD thesis, University of Michigan, 2006.

[57] C. Lingus. Analytical test case's for neutron and radiation transport codes. In *Second Conference on Transport Theory*, pages 655–659, Los Alamos, New Mexico, January 1971. United States Atomic Energy Commission - Division of Technical Information.

[58] Todd S. Palmer. *Curvilinear Geometry Transport Discretization in Thick Diffusive Regions*. PhD thesis, University of Michigan, 1993.

[59] Tom Brunner. Personal communication. Sep. 2015.

A Spatial Meshes

Included are various spatial meshes used in the test problems.

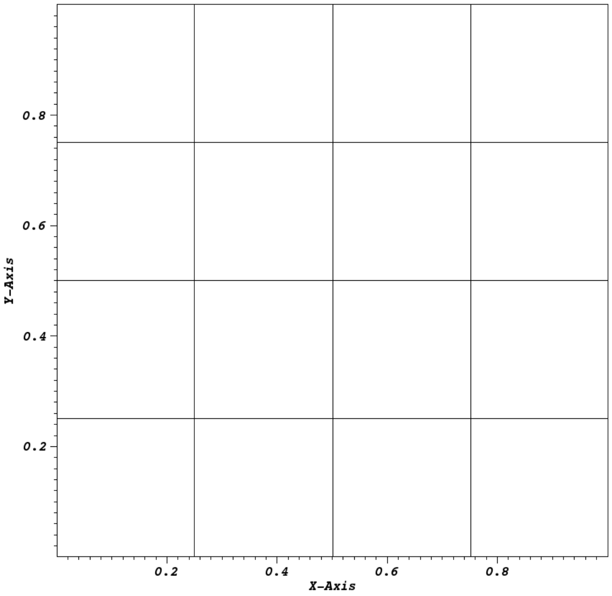

Figure 25: First order orthogonal mesh.

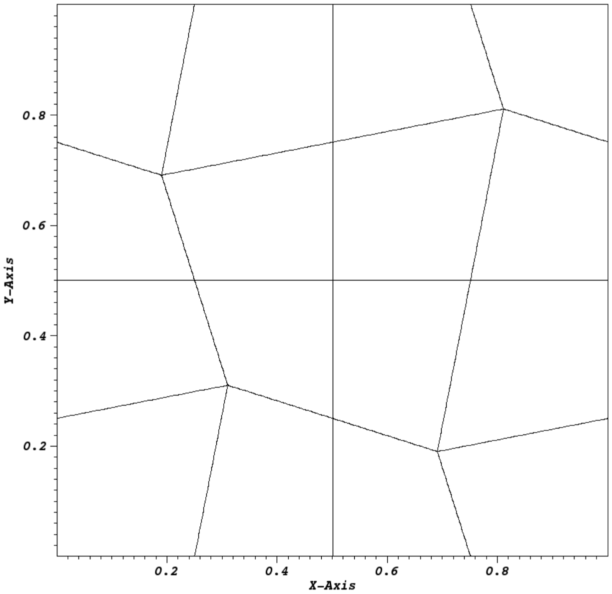

Figure 26: First order orthogonal mesh (Figure 25) transformed with first order edges.

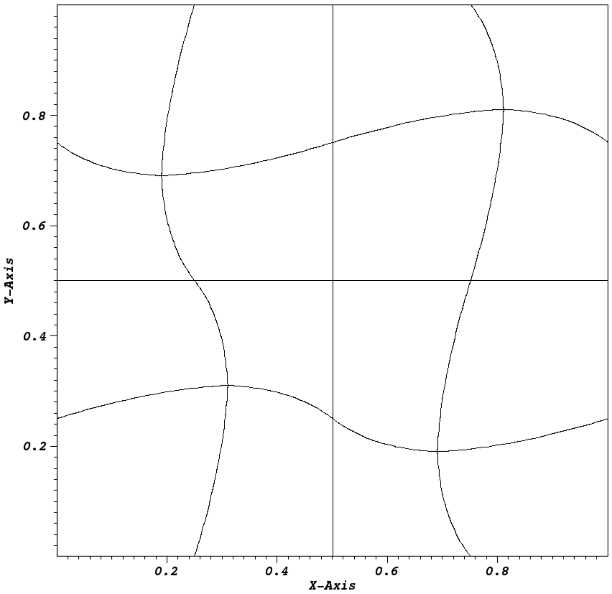

Figure 27: First order orthogonal mesh (Figure 25) transformed with second order curved edges.

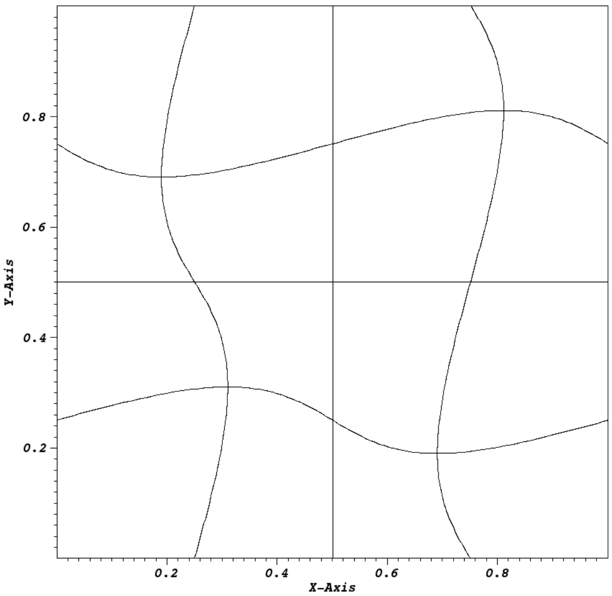

Figure 28: First order orthogonal mesh (Figure 25) transformed with third order curved edges.

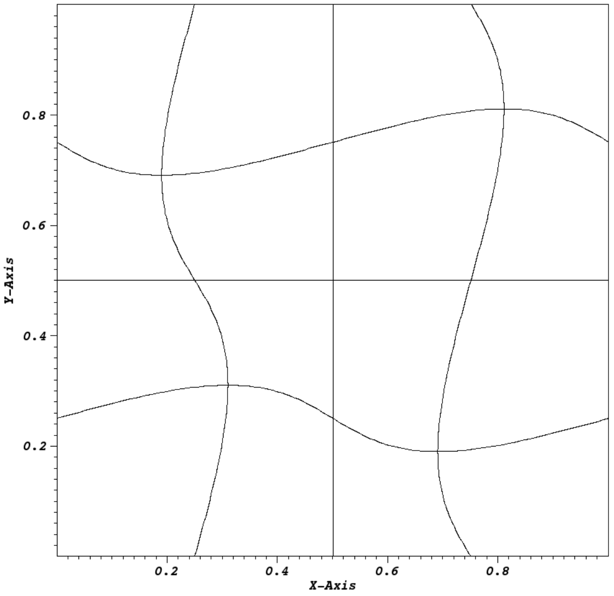

Figure 29: First order orthogonal mesh (Figure 25) transformed with eighth order curved edges.

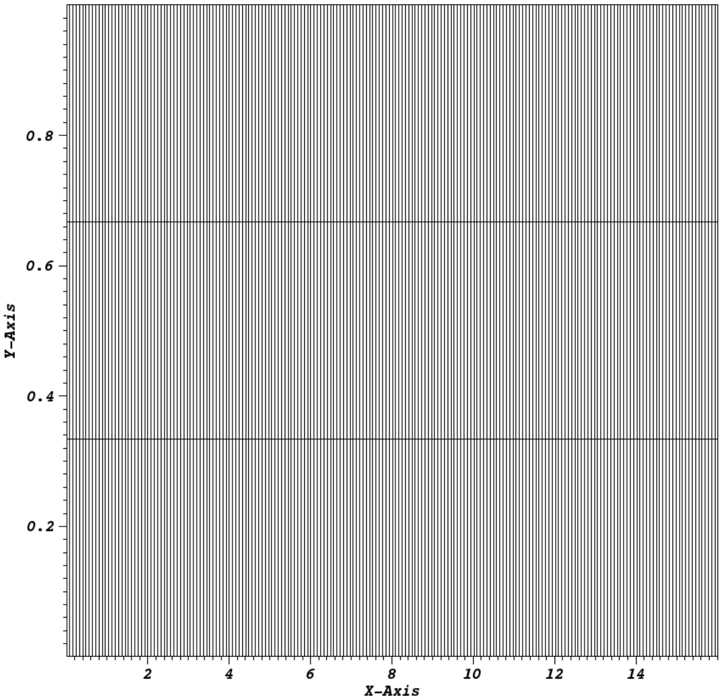

Figure 30: Mesh on $x \in (0, 16)$ with 200 cells in the x-direction and periodic boundary conditions on top and bottom.

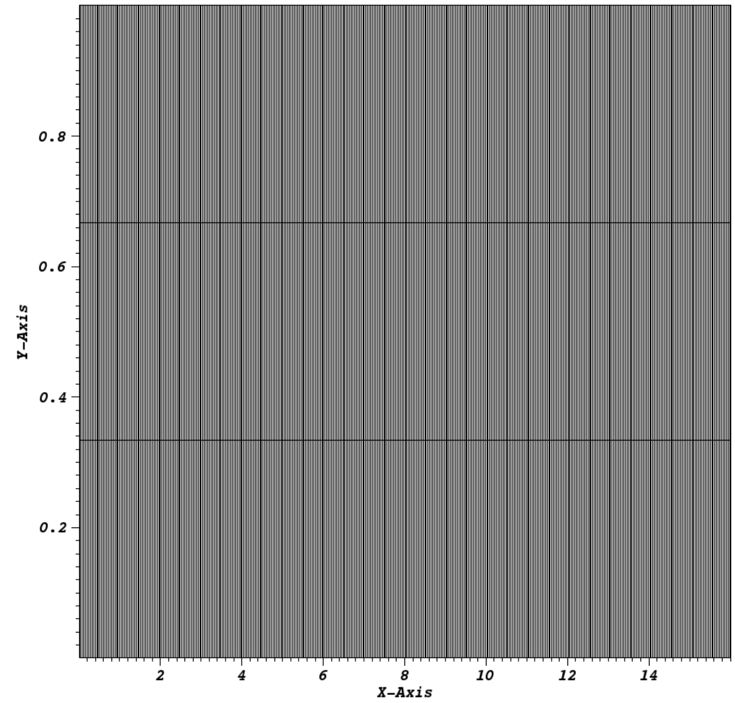

Figure 31: Mesh on $x \in (0, 16)$ with 400 cells in the x-direction and periodic boundary conditions on top and bottom.

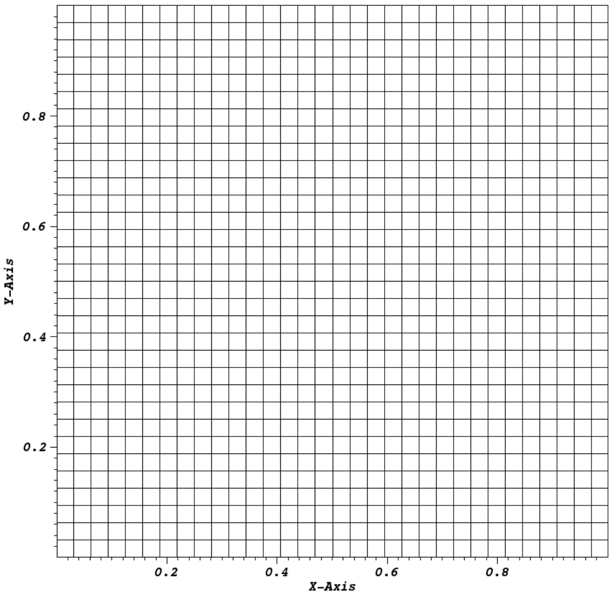

Figure 32: First order orthogonal mesh (Figure 25) refined to 256 mesh cells.

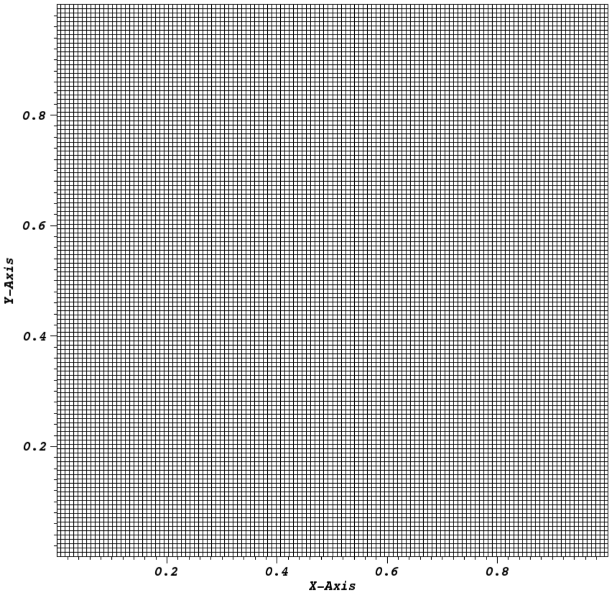

Figure 33: First order orthogonal mesh (Figure 25) refined to 16,384 mesh cells.

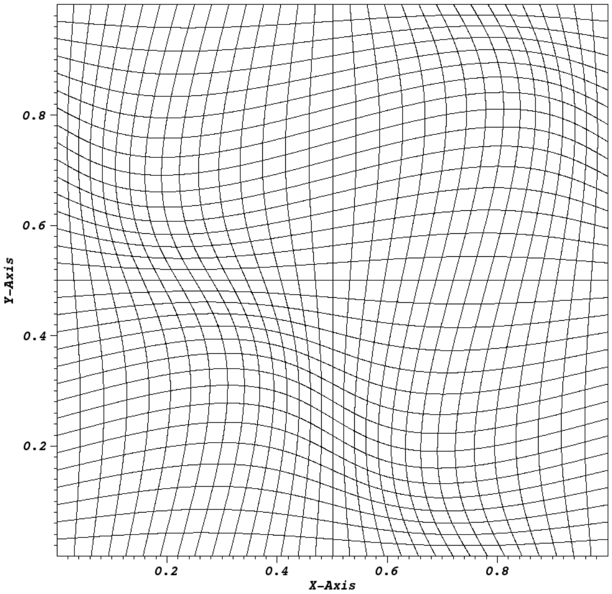

Figure 34: Third order mesh (Figure 28) refined to 256 mesh cells.

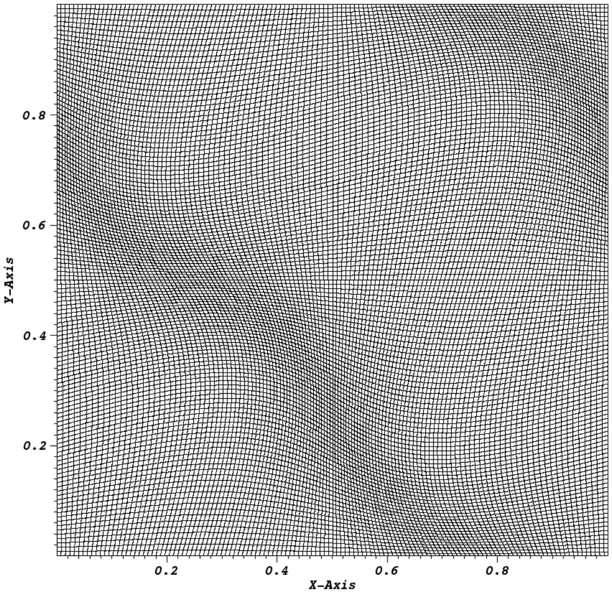

Figure 35: Third order mesh (Figure 28) refined to 16,384 mesh cells.

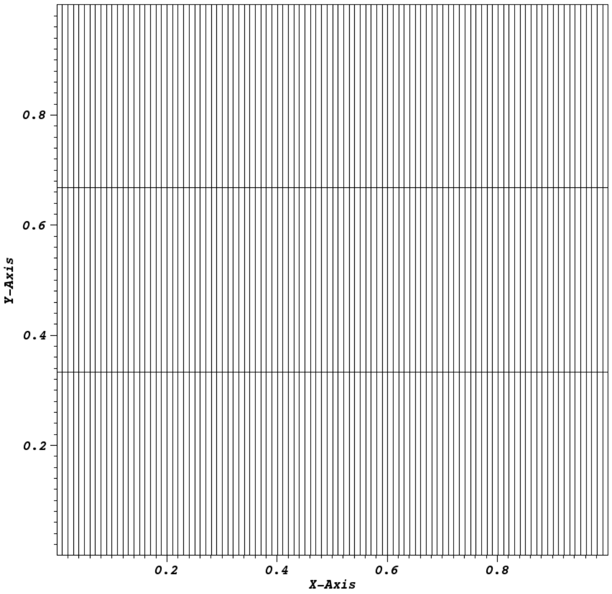

Figure 36: Mesh on $x \in (0, 1)$ with 200 cells in the x-direction and periodic boundary conditions on top and bottom.

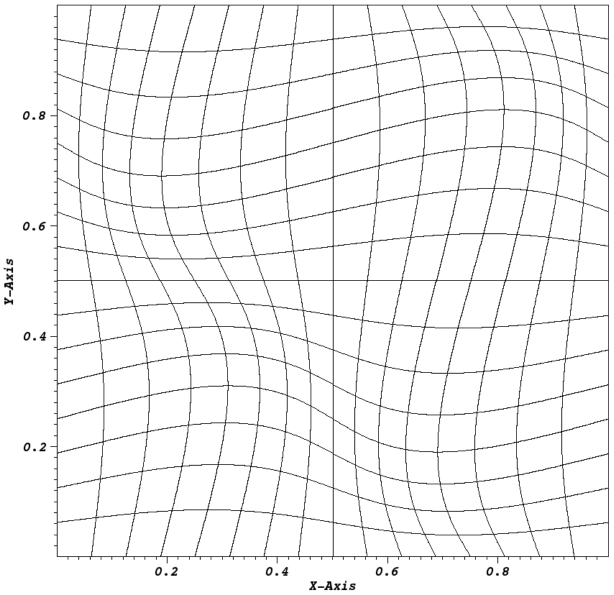

Figure 37: Eighth order mesh (Figure 29) refined to 256 mesh cells.

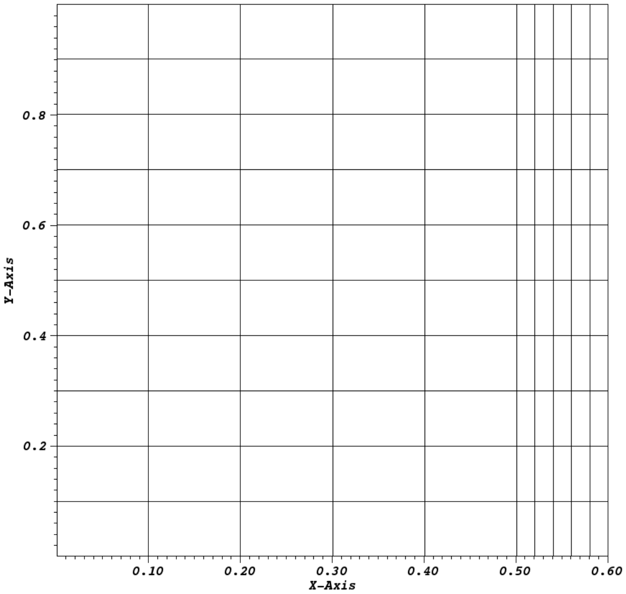

Figure 38: Mesh for Test Problem 6.

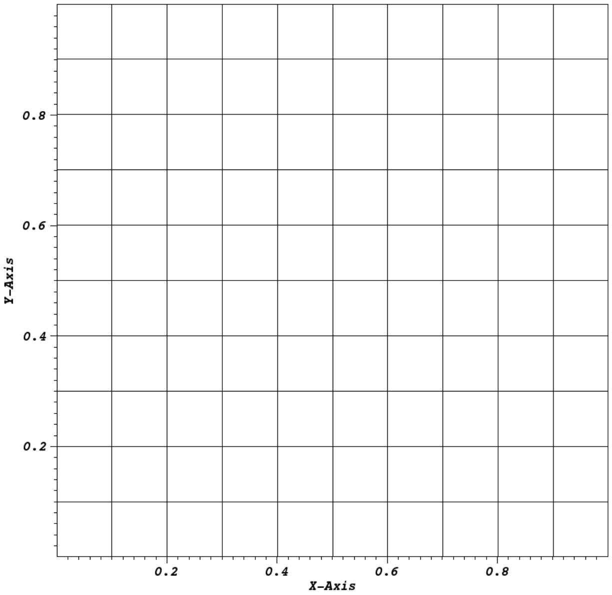

Figure 39: Mesh for Test Problem 7.

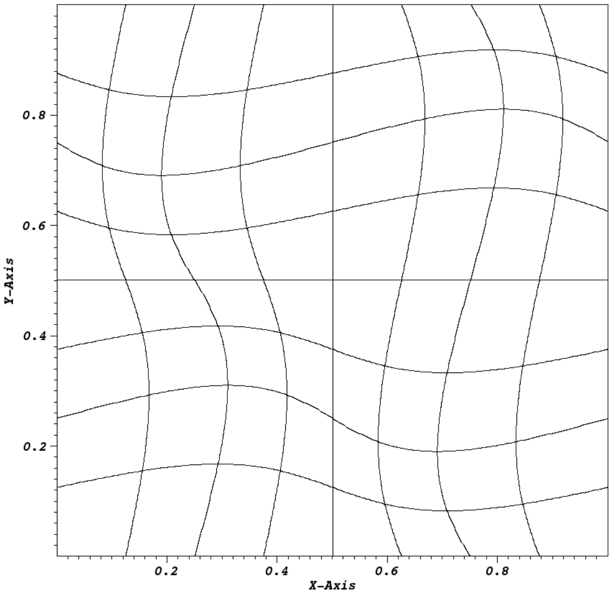

Figure 40: Second order mesh (Figure 27) refined to 64 mesh cells.